

Visualization Analysis of Pt and Co Species in Degraded Pt₃Co/C Electrocatalyst Layers of a Polymer Electrolyte Fuel Cell Using a Same-View Nano-XAFS/STEM-EDS Combination Technique

Shinobu Takao,^a Oki Sekizawa,^{a,b} Kotaro Higashi,^a Gabor Samjeské,^c Takuma Kaneko,^a Tomohiro Sakata,^a Takashi Yamamoto,^d Tomoya Uruga,^{a,b} and Yasuhiro Iwasawa^{a,e}*

^a Innovation Research Center for Fuel Cells, The University of Electro-Communications, Chofugaoka, Chofu, Tokyo 182-8585, Japan

^b Japan Synchrotron Radiation Research Institute, Spring-8, Sayo, Hyogo 679-5198, Japan

^c Department of Chemistry, Graduate School of Science, Nagoya University, Chikusa, Nagoya, Aichi 464-8602, Japan

^d Department of Mathematical and Material Sciences, Faculty of Integrated Arts and Sciences, The University of Tokushima, Minamijosanjima, Tokushima 770-8502, Japan

^e Department of Engineering Science, Graduate School of Informatics and Engineering, The University of Electro-Communications, Chofugaoka, Chofu, Tokyo 182-8585, Japan

ABSTRACT

In order to obtain a suitable design policy for the development of a next-generation polymer electrolyte fuel cell, we performed a visualization analysis of Pt and Co species following aging and degradation processes in MEA, using a same-view nano-XAFS–STEM/EDS technique that we developed to elucidate durability factors and degradation mechanisms of a MEA Pt₃Co/C cathode electrocatalyst with higher activity and durability than a MEA Pt/C. In the MEA Pt₃Co/C, after 5,000 ADT-rec (rectangle accelerated durability test) cycles, unlike the MEA Pt/C, there was no oxidation of Pt. In contrast, Co oxidized and dissolved over a wide range of the cathode layer

(~70% of the initial Co amount). The larger the size of the cracks and pores in the MEA Pt/C, and the smaller the ratio of Pt/ionomer of cracks and pores, the faster is the rate of catalyst degradation. In contrast, there was no correlation between the size or Co/ionomer ratio of the cracks and pores and the Co dissolution of the MEA Pt₃Co/C. It was shown that Co dissolved in the electrolyte region had an octahedral Co²⁺-O₆ structure, based on a 150 nm × 150 nm nano-XAFS analysis. It was also shown that its existence suppressed the oxidation and dissolution of Pt. The MEA Pt₃Co/C after 10,000 ADT-rec cycles had many cracks and pores in the cathode electrocatalyst layer, and about 90% of Co had been dissolved and removed from the cathode layer. We discovered a metallic Pt-Co alloy band in the electrolyte region of 300–400 nm from the cathode edge, and square planar Pt²⁺-O₄ species and octahedral Co²⁺-O₆ species in the area between the cathode edge and the Pt-Co band. Pt and Co chemical species in the Pt₃Co/C cathode electrocatalyst in the MEA during the deterioration process, and a fuel cell deterioration suppression process by Co, were visualized for the first time at the nano scale using the same-view nano-XAFS–STEM/EDS combination technique that can measure the MEA under humid N₂ atmosphere, while maintaining the working environment for a fuel cell.

Keywords: Visualization analysis, Same-view nano-XAFS–STEM/EDS combination technique, Pt and Co chemical species maps, Dissolved Pt²⁺ and Co²⁺ maps, PEFC Pt₃Co/C degradation process.

INTRODUCTION

Polymer electrolyte fuel cells (PEFCs) have attracted much attention as one of the most efficient clean energy generation systems to achieve an environmentally friendly, sustainable, and fossil-fuel-free society, realizing low or even zero emissions; they are considered to be suitable for automotive applications due to the high power density at low temperatures. For widespread commercialization of PEFC vehicles, remarkable improvements in both oxygen reduction reaction (ORR) activity and durability of cathode electrocatalysts are indispensable for reducing the cost of PEFC stacking and increasing the long-term durability of PEFC.¹⁻²² To understand and elucidate the key issues and mechanisms of the performance and degradation of PEFCs, *in situ/operando*

and *ex situ* characterization techniques, which can validate catalyst fabrications and prove fundamental issues in the development of next-generation PEFCs, are mandatory, and in particular, it is necessary to observe directly and spectroscopically the degradation process of cathodes in PEFCs.²³⁻²⁶

In situ time-resolved X-ray absorption fine structure (XAFS) techniques are very powerful for *in situ/operando* and element-selective investigation of electronic states and local coordination structures and the fluctuations (structural kinetics and dynamics) of cathode electrocatalysts in the membrane-electrode assembly (MEA) under PEFC operating conditions, which are regarded to be relevant to ORR performance and durability of MEA electrocatalysts.²⁷⁻³⁹ Such issues cannot be obtained by alternative analysis techniques. Nevertheless, the information is averaged in an area, larger than ten-micrometers of the cathode irradiated with non-focusing X-rays. The key elementary reaction and degradation processes of the cathode in MEA, which regulates ORR performance and durability of PEFC, have been visualized to occur heterogeneously in the space of the cathode layer using a three-dimensional (3D) Laminography.⁴⁰ Recently, the cathode degradation mechanism has become a more serious issue, and hence, the nanoscopic spatial place and mechanism of the dissolution and deterioration of cathode electrocatalysts in MEAs should be investigated to develop next-generation PEFCs with high performance and durability. To ascertain the degradation process of MEA cathode catalysts under PEFC working conditions, an *operando* 3D tomography (CT) –hard X-ray absorption fine structure (XAFS) imaging technique has been developed and applied to 3D visualization of MEA Pt/C and Pt₃Co/C cathodes.⁴¹⁻⁴⁶ The technique has provided new insight into the spatially heterogeneous issue and mechanism for the ORR property and degradation of Pt/C and Pt-M alloy/C cathode electrocatalyst layers in PEFCs. Imaging techniques using X-rays as a probe, such as X-ray absorption spectro-microscopy,⁴⁷⁻⁴⁹ scanning transmission X-ray microscopy,^{50,51} X-ray diffraction imaging,^{52,53} X-ray spectro-ptychography,^{54,55} and atom probe tomography⁵⁶ have also recently been applied to functional materials.

We have succeeded in mapping Pt chemical species in Pt/C cathode catalyst layers by using a scanning nano-XAFS mapping method and have obtained new insight into nano-spatial information concerning the site-preferential oxidation and leaching of Pt cathode nanoparticles in degraded PEFCs.⁵⁷ More recently, we have developed a new same-view combination technique of

nano XAFS and STEM-EDS under humid N₂ atmosphere using a new same-view stacking membrane cell and have also succeeded in performing same-view nano-XAFS and STEM-EDS imaging for MEA Pt/C cathode electrocatalyst layers.⁵⁸⁻⁶⁰ The complementary nano-XAFS and STEM-EDS imaging methods prompted the discovery of unprecedented aspects of the spectroscopic, chemical and morphological visualization of the leached Pt²⁺ oxidation species and detached metallic Pt nanoparticles in the degradation process of MEA Pt/C cathode electrocatalysts^{58,59} and elucidated the site-selective area, sequence and relationship of the degradations of Pt nanoparticles and carbon support in the MEA Pt/C cathode layer.⁶⁰

In this study, the same-view nano XAFS-STEM/EDS combination technique was further extended to include a nano-scale visualization analysis of Pt and Co species in degraded MEA Pt₃Co/C cathode electrocatalysts. We have visualized the high durability of metallic Pt species in the MEA Pt₃Co/C by sacrificial oxidation and dissolution of Co species for 10,000 ADT-rec (rectangle wave accelerated durability test) cycles, and we have also determined the formation of the Pt-Co alloy band in the electrolyte region, and the dissolution of square planar Pt²⁺-O₄ species and octahedral Co²⁺-O₆ species in the area between the Pt-Co band and the cathode layer edge in the degraded MEA Pt₃Co/C after 90% Co dissolution from the cathode layer for 10,000 ADT-rec cycles.

RESULTS AND DISCUSSION

Same-View Nano-XAFS/STEM-EDS Maps of MEA Pt₃Co/C After Aging (Conditioning).

The Pt₃Co/C cathode electrocatalyst is known to have higher activity and durability, which is especially important for a practical fuel cell, than the Pt/C. We performed electrochemical, TEM/STEM-EDS and XRD measurements during the degradation process, and, from the comparison with the Pt/C, examined characteristics of Pt₃Co/C degradation. Figure 1 shows the results of the electrochemical analysis and TEM/STEM-EDS analysis and XRD analysis performed during the degradation process. The catalyst particle diameter estimated by TEM (Figure 1A) increased as the number of ADT-rec cycles increased for both Pt₃Co/C and Pt/C. In response to the growth of catalyst particles, the rate of reduction in the particle surface area, geometrically estimated from particle size increase, was higher in the Pt/C than the Pt₃Co/C (Figure 1B). Reduction of electrochemically active surface area (ECSA, Figure S1 and Table S1

in Supporting Information) in the Pt/C catalyst, obtained from a hydrogen desorption peak of CV, was almost the same as the reduction in the particle surface area obtained from catalyst particle diameter (Figure 1C). However, in the Pt₃Co/C, compared to the rate of reduction in particle surface area obtained from the increase in catalyst particle diameter, the rate of reduction of ECSA was notably lower, and these two were not consistent. As shown in Figure 1C, the rate of reduction in the catalyst surface area, obtained from the particle diameter, was 24% after 5,000 ADT-rec cycles and 47% after 10,000 ADT-rec cycles. In contrast, the rate of reduction in ECSA was only 8% after 5,000 ADT-rec cycles and remained at 23% after 10,000 ADT-rec cycles (Figure S1 and Table S1). The rate of reduction in the maximum power density due to the deterioration of ADT-rec (Figure 1D and Figure S1) was smaller in the Pt₃Co/C in comparison to the Pt/C, e.g. 0.3 (reduction rate of Pt₃Co relative to that of Pt/C) after 5,000 ADT-rec cycles and 0.4 (reduction rate of Pt₃Co/C relative to that of Pt/C) after 10,000 ADT-rec cycles, and the Pt₃Co/C had higher durability than the Pt/C. This suggests that the nanoparticle surface in the Pt₃Co/C is different from the Pt/C. Figure 1E indicates that as the number of ADT-rec cycles increases more Co is dissolved from the Pt₃Co/C, e.g. 70% after 5,000 ADT-rec cycles and 90% after 10,000 ADT-rec cycles. Figure S2 shows the changes in XRD pattern due to the ADT-rec process. Catalytic metal particle diameters calculated from XRD were consistent with particle diameters calculated from TEM for the Pt/C (Figure 1A). In contrast, such consistency only occurred with the Pt₃Co/C after aging

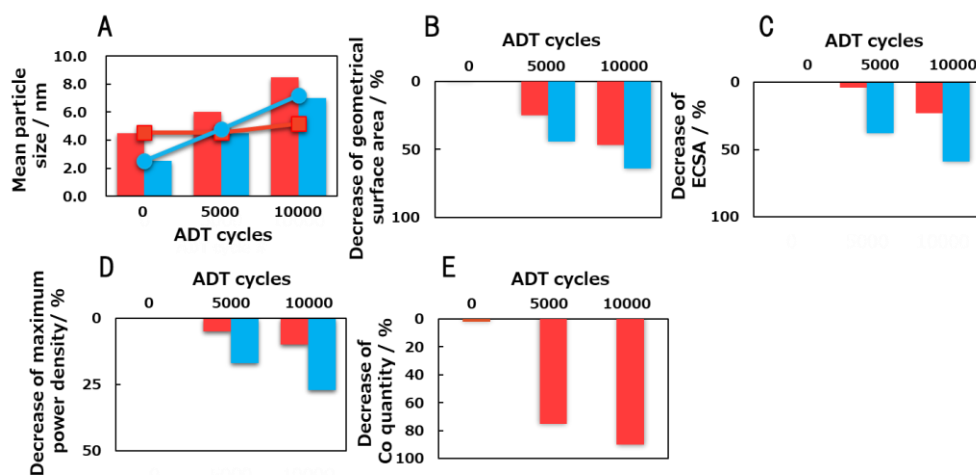


Figure 1. Degradation behavior of MEA Pt₃Co/C (red) and MEA Pt/C (blue) by ADT-rec cycles (0, 5,000, and 10,000 cycles). (A) Mean catalyst particle sizes estimated by TEM (bars) and XRD (lines with circles & squares)), (B) morphological surface areas calculated from TEM results in (A), (C) electrochemical active surface areas (ECSA), (D) maximum power densities, and (E) Co quantity at the cathode in MEA Pt₃Co/C.

(before ADT-rec cycles) and not in deteriorated samples after the ADT-rec cycles (Figure 1A). Particle diameter calculated from XRD was smaller than catalyst particle diameter calculated with TEM. In other words, it indicates that the surface Pt layer of the Pt₃Co/C was disordered during the deterioration process. In addition, Table S2 shows the result of examining the crystal surface orientation of the Pt₃Co/C and Pt/C. Both Pt₃Co/C and Pt/C had (111) orientation, and there was no notable change during the deterioration process. Thus, difference in activity and durability of the Pt₃Co/C and Pt/C was not due to variations in the crystal surface.

Activity and durability of the MEA Pt₃Co/C electrode catalyst are not necessarily the same for all Pt₃Co nanoparticles in the cathode layer. Specifically, degradation in the MEA has been reported to be spatially heterogeneous.^{40-42,45,46} We have developed a same-view nano-XAFS/STEM-EDS combination technique that performs an analysis of chemical state via nano-XAFS and have performed an analysis of the shape and elements using STEM/EDS on the same location of the same MEA sample, and have visualized the degradation process of the MEA Pt/C cathode electrocatalyst.⁵⁸⁻⁶⁰ Figure 2 shows the results of the measurement and analysis of the bonding structure and electronic state of the MEA Pt₃Co/C cathode before and after aging (before ADT-rec cycle), and the related spatial information, after applying the same-view nano-XAFS/STEM-EDS combined technique. As for the amount of Pt and Co, we performed linear combination fitting of the Lorentzian function and the arctangent function in XANES spectra (Pt: 11.550–11.600 keV, Co: 7.700–7.800 keV), and obtained the values for 11.600 keV or 7.760 keV of the calculated arctangent function. Valence of Pt was acquired from an approximation equation obtained from a linear fitting of the area of the white line for the reference samples, Pt⁰, PtO, and PtO₂, using the area of the Lorentzian function determined in the aforementioned analysis as the white line peak area. Since Co K-edge XANES and EXAFS of Co ions in the polymer electrolyte membrane after 5,000 ADT-rec cycles were consistent with those of [Co(H₂O)₆]²⁺ (Figure S3), valence of Co was obtained by performing a linear combination analysis of the Pt₃Co alloy (Pt₃Co alloy plate, TKK) and [Co(H₂O)₆]²⁺ in the XANES spectra and using its compositional ratio. A STEM image of a wide area (50 μm × 20 μm) (Figure 2A), the map of Pt content (Figure 2B), and the map of Co content (Figure 2C) showed that in the cathode catalyst layer of the aging MEA Pt₃Co/C prior to the ADT-rec process, C support, Pt, and Co were uniformly distributed. In addition, the map for Pt valence (Figure 2D) and Co valence (Figure 2E) showed that valence of Pt and Co were 0 and +0.2 (±0.1), respectively for the whole cathode electrocatalyst layer. The map of Co²⁺ content

(Figure 2F), calculated from the product of mole fractions of Co^{2+} species obtained from the maps of Co content and valence, shows that there was an extremely small amount of Co^{2+} in the whole cathode catalyst layer. Co^{2+} , which exists even if extremely small in quantity, was likely dissolved

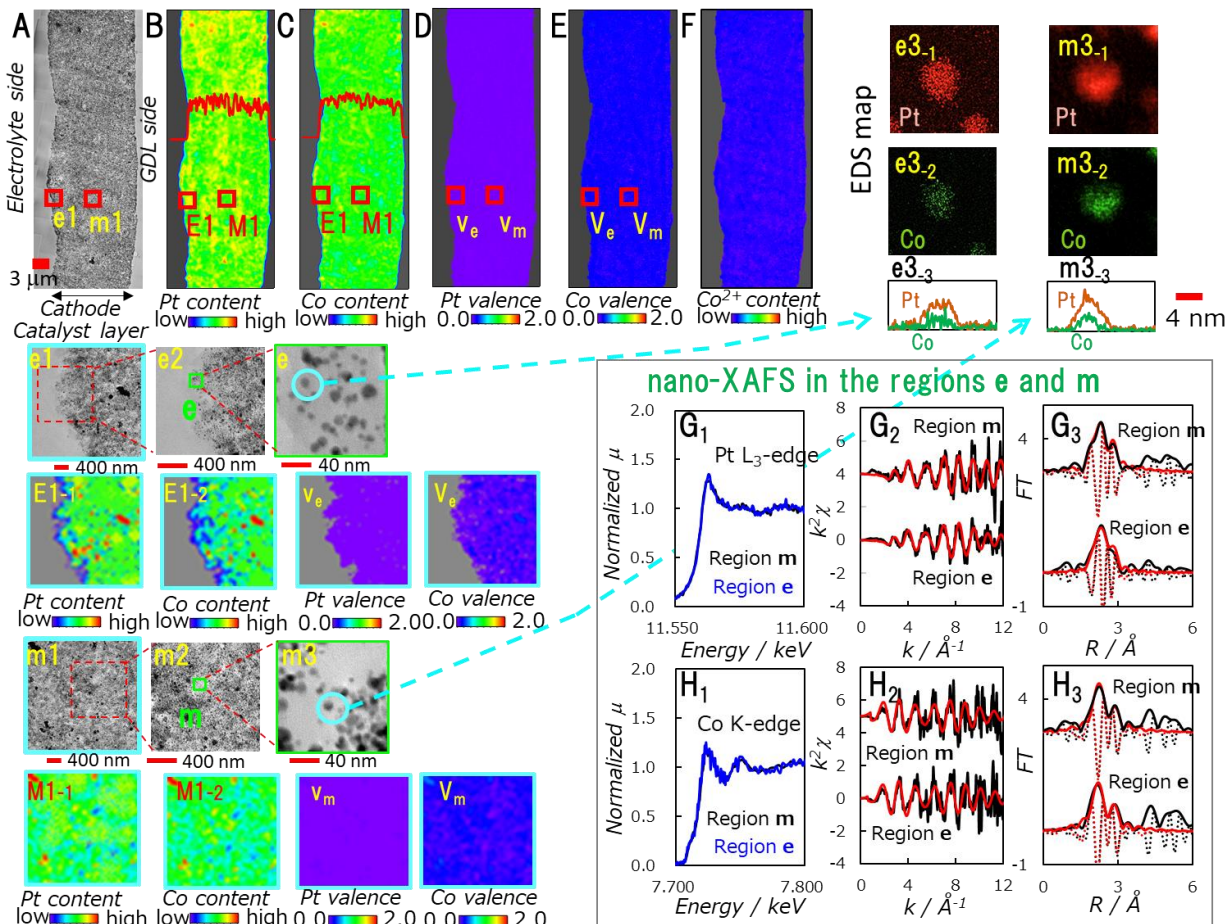


Figure 2. Same-view nano-XAFS and STEM/EDS results for the MEA Pt₃Co/C cathode catalyst layer after aging (before ADT-rec). Nano-XAFS data: B-F, E1₁ & -₂, v_e, V_e, M1₁ & -₂, v_m, V_m, G₁-G₃, and H₁-H₃. STEM/EDS data: A, B (line profile), C (line profile), e1, e2, e, m1, m2, m, e3₁₋₃, and m3₁₋₃. A: STEM image, B: Pt content map and EDS line profile, C: Co content map and Co line profile (the maximum amount of Co is normalized to the maximum amount of Pt, for easy viewing), D: Pt valence map, E: Co valence map, F: Co^{2+} content map. E1, E1, v_e and V_e: boundary region between the cathode catalyst layer and electrolyte (3 μm x 3 μm). m1, M1, v_m and V_m: middle region of the cathode catalyst layer (3 μm x 3 μm). e3₁ – e3₃: Pt EDS map, Co EDS map and Pt & Co line profiles for a single catalyst particle in the region e, respectively. m3₁ – m3₃: Pt EDS map, Co EDS map and Pt & Co line profiles for a single catalyst particle in the region m, respectively. G₁ – G₃: Pt L₃-edge XANES, EXAFS oscillations (black: observed; red: curve fitted) and their associated Fourier transforms (black solid lines: observed; black dotted lines: imaginary part; red solid and dotted lines: curve fitted, respectively) in the regions e (150 nm x 150 nm) and m (150 nm x 150 nm). H₁ – H₃: Co K-edge XANES, EXAFS oscillations (black: observed; red: curve fitted) and their associated Fourier transforms (black solid lines: observed; black dotted lines: imaginary part; red solid and dotted lines: curve fitted, respectively) in the regions e (150 nm x 150 nm) and m (150 nm x 150 nm), respectively.

from the Pt₃Co/C cathode during the aging process. In our previous studies of MEA Pt/C, the boundary cathode layer with the electrolytes was heavily deteriorated while the center of the cathode layer was relatively light. Hence, we visualized the central area of the cathode and the boundary between the cathode and electrolytes in the MEA Pt₃Co/C sample. E1-1, E1-2, v_e, and V_e in Figure 2 show the results of the same-view nano-XAFS–STEM/EDS for the microscopic areas e1, E1, v_e and V_e in a 3 μm × 3 μm area (Figure 2A-E) at the electrolyte boundary in the cathode electrocatalyst layer. In addition, m1, M1-1, M1-2, v_m, and V_m, seen in Figure 2, show the results of the same-view nano-XAFS–STEM/EDS for the 3 μm × 3 μm area near the center of the cathode catalyst layer (Figure 2A-E). The Pt content, Co content, Pt valence, and Co valence all had relatively uniform distribution.

Furthermore, we present nano-XANES (G₁ (Pt L₃-edge) and H₁ (Co K-edge) in Figure 2) and nano-EXAFS oscillations (G₂ (Pt L₃-edge) and H₂ (Co K-edge) in Figure 2), and their Fourier transform (FT) (G₃ (Pt L₃-edge) and H₃ (Co K-edge) in Figure 2) of a 150 nm × 150 nm area (**e** and **m**) in the 3 μm × 3 μm. Table 1 shows structural parameters obtained from the EXAFS curve fitting analysis in R space. Since the Pt valence map (Figure 2D) shows the Pt valence was zero at the boundary with the electrolytes and at the center, we obtained structural parameters by performing curve-fitting of two waves (Pt-Pt and Pt-Co) in the Pt L₃-edge nano-EXAFS analysis (Table 1). In fact, with three waves including Pt-O, the Pt-O coordination number (CN_{Pt-O}) and Debye Waller factor (σ²_{Pt-O}) both became negative, thus failing to provide reasonable fitting results (Table S3). In contrast to the Pt-Pt bond distance 0.273 nm (±0.001 nm) and Pt-Co bond distance 0.267 nm (±0.001 nm), Pt and Co did not form uniform alloy nanoparticles. Co K-edge nano-EXAFS analysis also showed that the bond lengths of Co-Pt and Co-Co were different (0.268 nm (±0.001 nm) and 0.265 nm (±0.002 nm), respectively), indicating that intermetallic compounds were formed, instead of random alloy, around the Co atoms. In the aging (conditioning) of MEA Pt₃Co/C, prior to deterioration, not only bond length but CN_{Pt-Pt}, CN_{Pt-Co}, CN_{Co-Pt}, CN_{Co-Co}, and CN_{Co-O} all had nearly identical values in the edge and center areas of the cathode layer, showing that the aging MEA Pt₃Co/C cathode layer was uniform. From the EDS line profiles e3-3 and m3-3 in Figure 2, we can see that the aging process leads to the dissolution of Co from the Pt₃Co nanoparticle surface, forming a Pt surface layer (shell) and creating core-shell-type nano particles. This result is consistent with previous studies.⁶¹⁻⁶³ Based on the ratio of CN_{Pt-Co} and CN_{Pt-Pt} from

Pt L₃-edge EXAFS (Table 1), the mean Co/Pt composition for the entire catalyst particles was about 1/3.6. Based on the ratio of CN_{Co-Co} and CN_{Co-Pt} from Co K-edge EXAFS, the mean composition of Co/Pt in the core of the catalyst particles was about 1/2. Therefore, the calculation suggests that the Pt shell consisted of two layers. STEM-EDS analysis (Figure S4) indicates that the shell layer structure consisted of roughly two Pt layers. We put this aging MEA Pt₃Co/C through a 5,000 cycle and a 10,000 cycle of 0.6-1.0 V ADT-rec and performed a visualization analysis of the degradation phenomenon using the same-view nano-XAFS–STEM/EDS (reported in detail in the following sections).

Table 1. Curve fitting results of the EXAFS data for the MEA Pt₃Co/C cathode electrocatalysts in the regions **e** and **m** (150 nm x 150 nm) and in the electrolyte region (150 nm x 150 nm) after aging (before ADT-rec) (Figure 2), 5,000 ADT-rec cycles (Figure 3) and 10,000 ADT-rec cycles (Figure 7).

Pt L ₃ -edge	after aging				after 5000 ADT cycles				after 10000 ADT cycles			
	Region e	error	Region m	error	Region e	error	Region m	error	Region e	error	Region m	error
CN _{Pt-Pt}	8.4	2.2	8.3	2.0	10.0	2.2	9.5	2.1	2.2	3.0	11.5	2.0
R _{Pt-Pt/nm}	0.273	0.001	0.273	0.000	0.273	0.001	0.273	0.001	0.273	0.001	0.273	0.002
σ ² _{Pt-Pt}	0.0051	0.0012	0.0045	0.0022	0.0060	0.0018	0.0062	0.0032	0.0052	0.0022	0.0050	0.0020
CN _{Pt-Co}	2.2	1.2	2.4	1.1	0.2	1.0	0.6	2.0	0.2	3.2	0.1	1.0
R _{Pt-Co/nm}	0.267	0.001	0.267	0.000	0.266	0.001	0.265	0.001	0.266	0.015	0.265	0.005
σ ² _{Pt-Co}	0.0062	0.0024	0.0060	0.0022	0.0044	0.0020	0.0040	0.0021	0.0040	0.0122	0.0042	0.0102
CN _{Pt-O}									2.5	1.0	0.5	0.2
R _{Pt-O/nm}									0.199	0.003	0.199	0.001
σ ² _{Pt-O}									0.0050	0.0045	0.0053	0.0031
ΔE	5.3	2.4	5.5	1.2	4.0	2.0	5.0	2.9	5.2	2.5	5.0	2.9
R _f /%	1.5		1.0		2.8		2.9		1.8		1.8	

Co K-edge	after aging				after 5000 ADT cycles				Electrolyte	
	Region e	error	Region m	error	Region e	error	Region m	error	error	error
CN _{Co-Pt}	4.5	0.3	4.7	4.0	1.5	2.6	8.2	2.2	0.2	2.1
R _{Co-Pt/nm}	0.268	0.002	0.269	0.000	0.268	0.002	0.268	0.002	0.268	0.001
σ ² _{Co-Pt}	0.0017	0.0030	0.0022	0.0027	0.0032	0.0044	0.0032	0.0031	0.0300	0.0130
CN _{Co-Co}	2.2	0.4	2.5	4.0	0.8	2.3	1.4	3.8	0.0	2.2
R _{Co-Co/nm}	0.266	0.001	0.264	0.002	0.264	0.000	0.265	0.002	0.264	0.008
σ ² _{Co-Co}	0.0063	0.0045	0.0061	0.0043	0.0040	0.0032	0.0054	0.0008	0.0040	0.0210
CN _{Co-O}	0.5	0.3	0.5	0.4	4.3	1.2	0.1	3.1	5.7	1.3
R _{Co-O/nm}	0.210	fixed	0.210	fixed	0.210	fixed	0.210	fixed	0.210	0.001
σ ² _{Co-O}	0.0030	fixed	0.0030	fixed	0.0030	fixed	0.0030	fixed	0.0032	0.0022
ΔE	3.5	0.4	4.0	1.0	5.0	1.8	4.6	1.0	6.0	3.0
R _f /%	1.0		1.8		1.8		1.8		2.0	2.0

Same-View Nano-XAFS/STEM-EDS Maps After 5000 ADT-rec Cycles. Figure 3 shows the results of the same-view nano-XAFS/STEM-EDS visualization analysis for the MEA Pt₃Co/C cathode after 5,000 cycles of 0.6–1.0 V rectangle ADT. Various sizes of cracks and pores existed that were hardly observed in the Pt₃Co/C cathode layer in the aging sample, shown in Figure 3A. Cracks and pores in the cathode layer may be produced by carbon corrosion due to undesired

heterogeneous potential ramping and/or gasification during ADT cycles. There were also many cracks and pores in the area of the cathode located at a slight medial from the boundary edge with the electrolyte (Figure 3 A). In the area with the cracks and pores, the Pt content decreased slightly (Figure 2 B and Figure 3 B), and the Co content decreased by approximately 70% (Figure 1E, Figure 2C and Figure 3C). The map of Pt valence (Figure 3D) shows that there was no oxidation of Pt in the whole cathode electrocatalyst layer. This result is notably different from the oxidation behavior of Pt recorded in our previous study on ADT-rec processed MEA Pt/C and the MEA Pt/C cathode electrocatalyst after 5,000 ADT-rec cycles from the present study (Figure 4C). In other words, in the MEA Pt/C after 5,000 ADT-rec cycles, Pt was oxidized in the area of large cracks and pores of 0.5 μm or larger and dissolved Pt^{2+} ions into the large cracks and pores were observed. There was a formation of a Pt band in electrolytes near the cathode edge (Figures 4A and 4B), and Pt^{2+} ions were found in the area between the cathode edge and the Pt band (Figure 4C). In the EXAFS analysis (Figures 4E and 4F) of the 150 nm \times 150 nm nano area (edge area e), Pt-O bond (0.205 nm) was observed and $\text{CN}_{\text{Pt-O}}$ was 3.2 ± 0.5 , indicating a Pt^{2+} species similar to a four-coordinated $\text{Pt}^{2+}\text{-O}_4$ (probably square planar) structure in the area of large cracks and holes previously reported.^{58,59} Other than in the area of cathode edge, many Pt^{2+} species were also observed (v_m in Figure 4) in the pores of the cathode layer (m1–m2 in Figure 4). In contrast, in the MEA $\text{Pt}_3\text{Co/C}$ after 5,000 ADT-rec cycles, there was no formation of a Pt band and the Pt atoms of the cathode were not at all oxidized (Figures 3A and 3B, and v_e and v_m in Figure 3D). Meanwhile, Co was oxidized in a wide area of the cathode (V_e and V_m in Figure 3E), and Co^{2+} ions were identified in the large cracks and pores in the area of the cathode near the edge (V_e in Figure 3E). It was also discovered that Co^{2+} ions were dissolved and distributed for 4 μm or more in the polymer electrolyte membrane (Figures 3C and 3E). In the Figure 2E depicting the aging sample (before the ADT-rec process), the whole cathode layer was uniform. In contrast, Figure 3E shows the map of heterogeneous valence of Co. Co^{2+} ions were found across the whole cathode electrocatalyst layer though the content varied (Figures 3E and 3F). Specifically, there were a large number of Co^{2+} ions from the boundary with electrolytes $\sim 4 \mu\text{m}$ into the cathode (Figure 3F). In contrast, the area toward GDL from the center of the cathode had many domains, in which metallic Co atoms with a mean valence close to zero existed.

We performed same-view nano-XAFS/STEM-EDS measurements for an area of $3\ \mu\text{m} \times 3\ \mu\text{m}$ in two typical locations with different degrees of degradation; for example, the edge against electrolytes (e1 in Figure 3A) and the central area of the cathode electrocatalyst layer (m1 in Figure

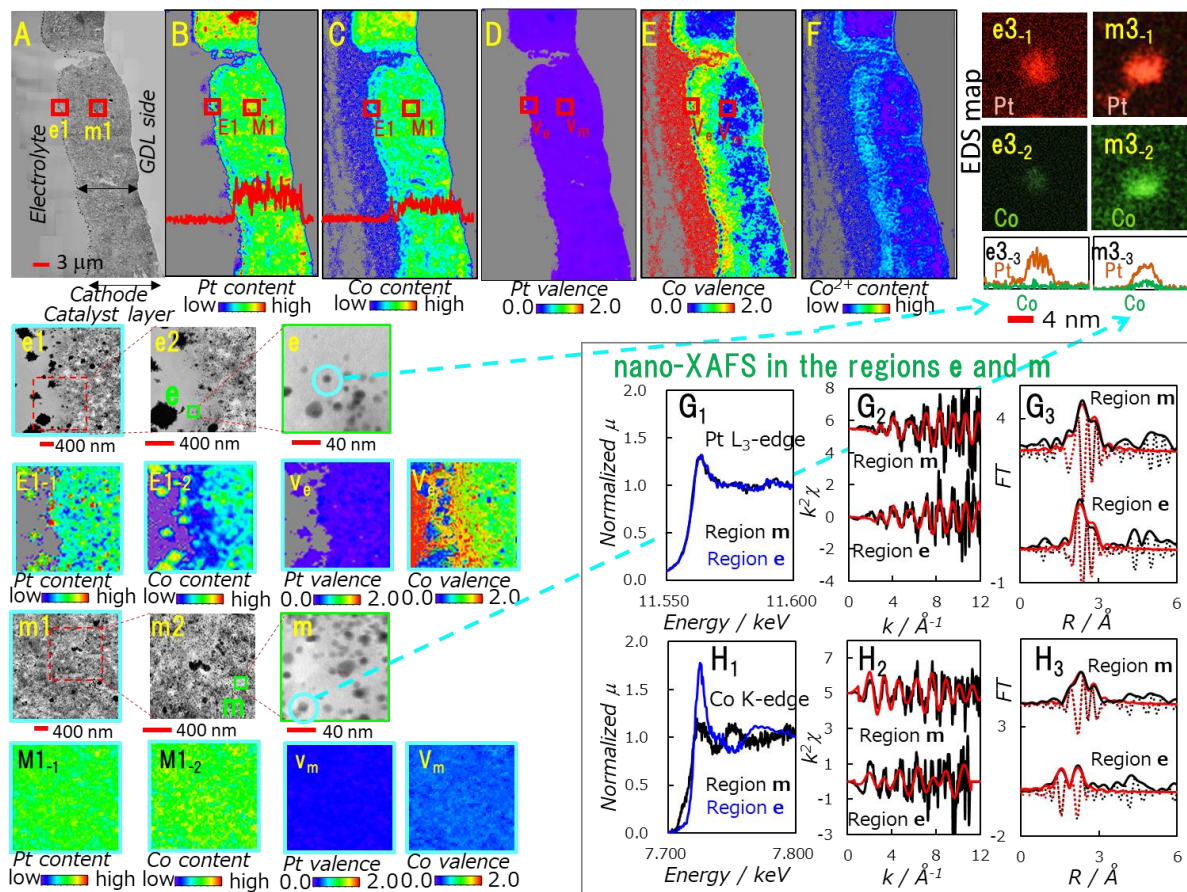


Figure 3. Results of the same-view nano-XAFS and STEM/EDS measurements of the MEA Pt₃Co/C cathode electrocatalyst layer after 5,000 ADT-rec cycles. nano-XAFS data: B-F, E1₁ & -₂, v_e, V_e, M1₁ & -₂, v_m, V_m, G₁-G₃, and H₁-H₃. STEM/EDS data: A, B(line profile), C(line profile), e1, e2, e, m1, m2, m, e3₁₋₃, and m3₁₋₃. A: STEM image, B: Pt content map and EDS line profile (decrease from Figure 2B), C: Co content map and EDS line profile (decrease from Figure 2C), D: Pt valence map, E: Co valence map, F: Co²⁺ content map (the same color bar in 3C). e1, E1, v_e and V_e: boundary region between the cathode electrocatalyst layer and electrolyte ($3\ \mu\text{m} \times 3\ \mu\text{m}$). m1, M1, v_m and V_m: middle region of the cathode electrocatalyst layer ($3\ \mu\text{m} \times 3\ \mu\text{m}$). e3₁₋₃–e3₃: Pt EDS map, Co EDS map and Pt & Co line profiles for a single catalyst particle in the region **e**, respectively. m3₁₋₃–m3₃: Pt EDS map, Co EDS map and Pt & Co line profiles for a single catalyst particle in the region **m**, respectively. G₁–G₃: Pt L₃-edge XANES, EXAFS oscillations (black: observed; red: curve fitted) and their associated Fourier transforms (black solid lines: observed; black dotted lines: imaginary part; red solid and dotted lines: curve fitted, respectively) in the regions **e** ($150\ \text{nm} \times 150\ \text{nm}$) and **m** ($150\ \text{nm} \times 150\ \text{nm}$). H₁–H₃: Co K-edge XANES, EXAFS oscillations (black: observed; red: curve fitted) and their associated Fourier transforms (black solid lines: observed; black dotted lines: imaginary part; red solid and dotted lines: curve fitted, respectively) in the regions **e** ($150\ \text{nm} \times 150\ \text{nm}$) and **m** ($150\ \text{nm} \times 150\ \text{nm}$), respectively.

3A). Results are shown in e_1 , E_{1-1} , E_{1-2} , v_e and V_e , and m_1 , M_{1-1} , M_{1-2} , v_m and V_m of Figure 3, respectively. In the area of cathode about ~ 400 nm from the electrolyte edge, the Co content decreased (E_{1-2}), where Co was dissolved into electrolytes as Co^{2+} ions (V_e). Meanwhile, although there was some heterogeneity in Pt distribution, there was little change in the Pt content (E_{1-1}), and the valence of Pt remained at zero (v_e). We presented XANES spectra at Pt L₃-edge (G_1) and Co K-edge (H_1) and EXAFS oscillations at Pt L₃-edge (G_2) and Co K-edge (H_2), and their Fourier transforms and curve fittings (G_3 (Pt L₃-edge) and H_3 (Co K-edge) for the $150 \text{ nm} \times 150 \text{ nm}$ nano area in the e and m areas in Figure 3 e2 and m2, respectively. Table 1 shows the structural parameters obtained from the EXAFS curve-fitting analysis. In addition, we performed particle analysis with STEM-EDS for the areas inside the nano areas (e and m) measured using nano-XAFS. Dissolution of Co from the Pt₃Co electrocatalyst particles was notable in the boundary containing electrolytes, but also occurred in the central area of the cathode electrocatalyst, where the number of Pt shell layers increased with dissolution of Co (Figure S5). In the central area of the cathode layer, the Co/Pt ratio for the overall nanoparticles was estimated as 1/15.8 via $\text{CN}_{\text{Pt-Pt}}$ and $\text{CN}_{\text{Pt-Co}}$ obtained from the Pt L₃-edge EXAFS analysis, and the Co/Pt ratio near the electrolyte edge of the cathode layer was estimated as 1/50. On the other hand, the Co/Pt ratio was 1/5.8 at the core of nanoparticles in electrocatalyst nanoparticles in the center of the cathode based on $\text{CN}_{\text{Co-Co}}$ and $\text{CN}_{\text{Co-Pt}}$ obtained from Co K-edge EXAFS analysis, and 1/1.9 in nanoparticles near the edge (Table 1). Therefore, the Pt shell layer of the core-shell nanoparticles near the cathode edge and near the center of the cathode was estimated to be seven layers and four layers, respectively. The Co/Pt ratio of the core, calculated from the aforementioned EXAFS analytical result, was larger than the composition calculated from EDS (0.15). This was because, in the EDS estimation, the mean Co/Pt includes the shell layer on the surface of particles, while in the Co K-edge EXAFS it analyzes the Co/Pt ratio of the core alone.

As shown in Table 1, even after 5,000 ADT-rec cycles, there were only Pt-Pt bonds (0.273 ± 0.001 nm) and Pt-Co bonds (0.265 ± 0.001 nm) in the nanoparticles at the boundary with the electrolytes and at the center of the cathode, and there were no Pt-O bonds observed. Similar to the aging MEA Pt₃Co/C, Pt was not oxidized, instead it maintained a metallic state. It exhibited a notable contrast to the MEA Pt/C that did not contain Co, where after 5,000 ADT-rec cycles, Pt was oxidized to Pt^{2+} ions and dissolved (Figure 4). As for Co, 5,000 ADT-rec cycles led to an 85% reduction in the amount of Co at the boundary with the electrolytes and a 60% reduction at the center of the cathode

layer. Remaining Co species showed Co-Pt bond (0.268 ± 0.002 nm) and Co-Co bond (0.265 ± 0.002 nm) in the center of the cathode layer, similar to the aging sample prior to ADT-rec. However, the coordination numbers of Co-Pt and Co-Co (CN_{Co-Pt} and CN_{Co-Co}) increased from 4.7 in the aging sample to 8.2, or decreased from 2.5 to 1.4, respectively. Furthermore, the coordination number of Co-O (CN_{Co-O}) was not identified in the range of error (Table 1). The results mean that, since Co was dissolved from the core of the nanoparticles and moved to the boundary with the electrolytes, the amount of Co in the core decreased, which in turn led to an increase in CN_{Co-Pt} and decrease in CN_{Co-Co} Co. In other words, dissolved Co^{2+} ions did not remain in the area around the original nanoparticles or pores but instead, rapidly moved away. In the samples following the 5,000 ADT-rec cycles the Co^{2+} ions were present in relatively large amounts in the area from the boundary

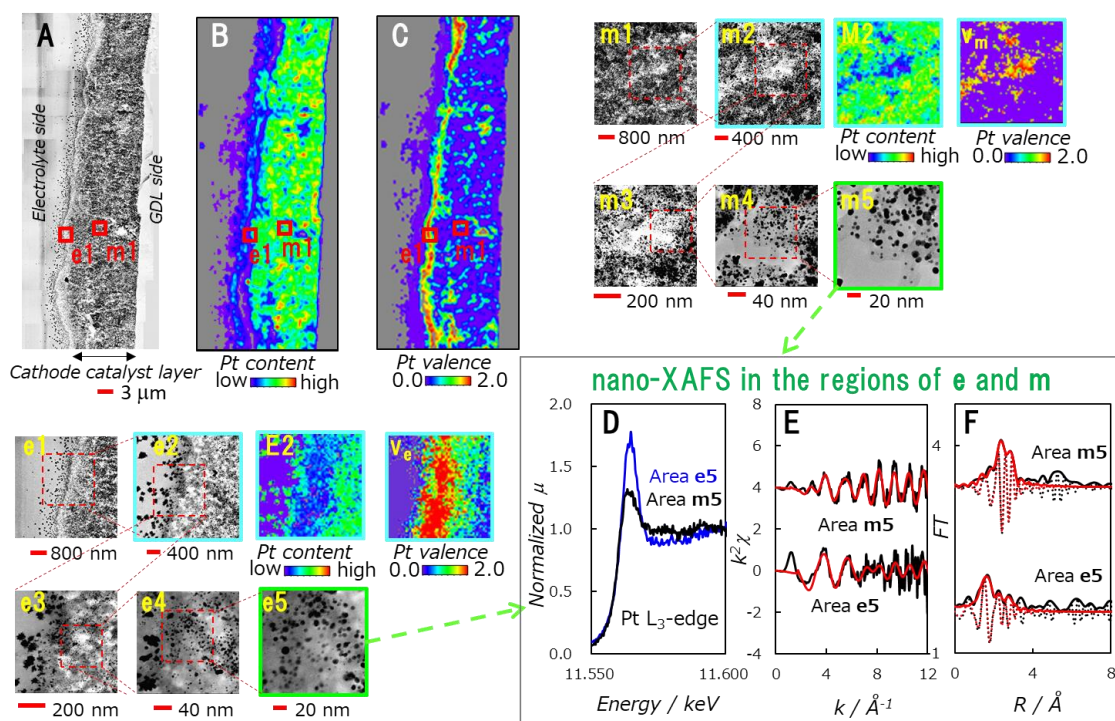


Figure 4. Results of nano-XAFS and STEM/EDS of the referential MEA Pt/C after 5,000 ADT-rec. Nano-XAFS data: B, C, E2, v_e , M2, v_m , and D-F. STEM/EDS data: A, e1-e4, e, m1-m5. A: STEM image, B: Pt content map, C: Pt valence map, e1-e5: STEM images for the boundary region between the cathode electrocatalyst layer and electrolyte, E2: Pt content map for e2, v_e : Pt valence map for e2, m1-m5: STEM image of the middle region of the cathode electrocatalyst layer. M2: Pt content map for m2, v_m : Pt valence map for m2, D: XANES of the boundary region (e5, 150 nm x 150 nm) and the middle region of the cathode electrocatalyst layer (m5, 150 nm x 150 nm), E: EXAFS oscillations of the boundary region (e5) and the middle region of the cathode electrocatalyst layer (m5) (black: observed; red: curve fitted), F: EXAFS Fourier transforms (black solid lines: observed; black dotted lines: imaginary part; red solid and dotted lines: curve fitted, respectively). For EXAFS curve fitting analysis, Δk : 3-12 \AA^{-1} , ΔR : 1.4 – 3.2 \AA .

with the electrolytes to approximately $\sim 4 \mu\text{m}$ inside the cathode (Figure 3F). In the nanoparticles near the cathode edge, $\text{CN}_{\text{Co-Pt}}$ and $\text{CN}_{\text{Co-Co}}$ remarkably decreased from 4.5 of the aging sample to 1.5 and from 2.2 to 0.8, respectively, and $\text{CN}_{\text{Co-O}}$ (Co-O: 0.210 nm) notably increased from 0.5 of the aging sample to 4.3. Near the edge, most Co atoms were oxidized to Co^{2+} (V_e in Figure 3). Furthermore, in the electrolyte region, up to $6 \mu\text{m}$ from the edge, $\text{CN}_{\text{Co-Pt}}$ or $\text{CN}_{\text{Co-Co}}$ was scarcely observed, indicating that Co^{2+} had dissolved to single ions and, since $\text{CN}_{\text{Co-O}}$ was 5.7 ± 1.3 , dissolved Co^{2+} ions had an octahedral structure (Table 1).

The Nano-XANES spectrum of the electrolyte region ($150 \text{ nm} \times 150 \text{ nm}$) was consistent with the XANES spectrum of $[\text{Co}(\text{H}_2\text{O})_6]^{2+}$ (Figure 5). In Figure 5, we present the XANES spectra of $\text{Co}(\text{acac})_3$, Pt_3Co alloy, Co_3O_4 , CoO and Co foil as reference materials for comparison. In the MEA, in addition to H_2O , there are Nafion ionomers; thus, its sulfonic group (Nf_{sulf}) may also be coordinated to Co^{2+} ; $[\text{Co}(\text{Nf}_{\text{sulf}})_x(\text{H}_2\text{O})_y]^{2+}$. Alternatively, sulfonate ions ($\text{Nf}_{\text{sulf}}^-$) may be stabilizing $[\text{Co}(\text{H}_2\text{O})_6]^{2+}$ as a counterion; $[\text{Co}(\text{H}_2\text{O})_6]^{2+}(\text{Nf}_{\text{sulf}}^-)_2$. These results indicate that during the 5,000 ADT-rec cycles, Co was preferentially oxidized and dissolved from the $\text{Pt}_3\text{Co}/\text{C}$ cathode and the

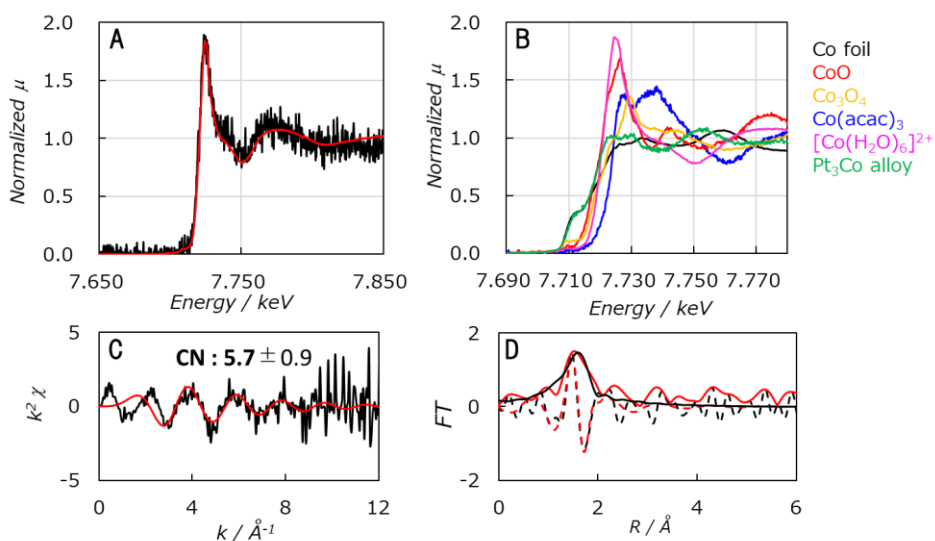


Figure 5. A: XANES spectrum of the $150 \text{ nm} \times 150 \text{ nm}$ electrolyte region $6 \mu\text{m}$ away from the boundary with the cathode electrocatalyst layer of the $\text{Pt}_3\text{Co}/\text{C}$ MEA after 5,000 ADT-rect cycles (black) and XANES spectrum of $[\text{Co}(\text{H}_2\text{O})_6]^{2+}$ (red), B: XANES spectra of the reference materials, C and D: EXAFS oscillations (black: observed; red: curve fitted) and Fourier transforms (black solid lines: observed; black dotted lines: imaginary part; red solid and dotted lines: curve fitted, respectively) of the $150 \text{ nm} \times 150 \text{ nm}$ electrolyte region in A (black: observed; red: curve fitted). For EXAFS curve fitting analysis, Δk : $3\text{--}12 \text{ \AA}^{-1}$, ΔR : $1.4\text{--}3.2 \text{ \AA}$.

dissolved Co^{2+} ions had octahedral structures, such as $[\text{Co}(\text{Nf}_{\text{sulf}})_x(\text{H}_2\text{O})_y]^{2+}$ and $[\text{Co}(\text{H}_2\text{O})_6]^{2+}$. Meanwhile, the oxidation and dissolution of Pt observed in the MEA Pt/C (Figure 4) were not observed in the MEA Pt₃Co/C (v_e and v_m in Figure 3D), where the metallic Pt surface of the fuel cell activity was maintained. Although the Pt shell layer was slightly thicker than the three-atom layers with bulk Pt properties and the amount of Co reduced, the oxidation and dissolution of Pt was suppressed. This may indicate that $[\text{Co}(\text{Nf}_{\text{sulf}})_x(\text{H}_2\text{O})_y]^{2+}$ and $[\text{Co}(\text{H}_2\text{O})_6]^{2+}$ adsorbed on the Pt shell surface, suppressing the oxidation and dissolution of Pt.⁶⁴ Alternatively, effective concentrations of Nf_{sulf} and $\text{Nf}_{\text{sulf}}^-$ of Nafion ionomers near the cathode edge and in the cracks and pores, which also stabilize Pt^{2+} and promote Pt dissolution from the carbon surface, were reduced by coordination to Co^{2+} ions, and as the result.⁵⁷⁻⁶⁰

Comparison of the Oxidation and Deterioration Factors of Pt and Co in MEA Pt₃Co/C and MEA Pt/C. We found that, in regard to the oxidation of Pt and dissolution of Pt^{2+} associated with the deterioration of the MEA Pt/C, there is a threshold for the size of cracks and pores and for the Pt/ionomer ratio; Pt^{2+} ions dissolved when the size of cracks and pores was higher than 500 nm,

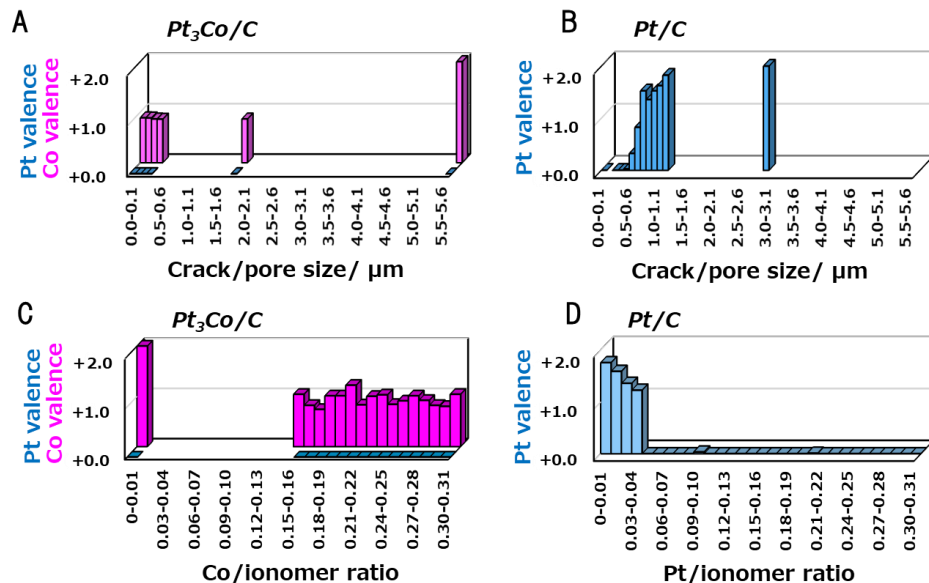


Figure 6. Relation of Co and Pt valences with the crack/pore size or Co/ionomer ratio at the cathode layer for the MEA Pt₃Co/C (A and C) after 5,000 ADT-rec cycles and relation of Pt valence with the crack/pore size or Pt/ionomer ratio at the cathode layer for the MEA Pt/C (B and D) after 5,000 ADT-rec cycles. A & C: Co valence (pink bar graph) and Pt valence (light blue bar graph).

while Pt in the size lower than 500 nm was metallic (detached as clusters/nanoparticles from carbon support), but Pt was not metallic and dissolved as Pt^{2+} ions when the Pt/ionomer ratio of cracks and pores was lower than 0.05.⁵⁹ Therefore, we were able to plot the correlation between oxidation and dissolution of Pt or Co, associated with ADT-rec deterioration of the MEA $\text{Pt}_3\text{Co}/\text{C}$, with the size of cracks and pores or Pt/ionomer in cracks and pores (Figure 6A and 6C). In the MEA $\text{Pt}_3\text{Co}/\text{C}$, in contrast to the behavior of Pt in the MEA Pt/C (Figure 6B and 6D), there was no oxidation of Pt after 5,000 ADT-rec cycles, and only oxidation of Co progressed (Co^{2+} generation) (Figures 6A and 6C). In other words, oxidation and dissolution of Pt were suppressed by the sacrificial oxidation of Co. In addition, the relationship between the size of cracks/pores and metal oxidation observed in the Pt/C was not observed in the $\text{Pt}_3\text{Co}/\text{C}$. Regardless of the size of cracks and pores, Co was non-selectively oxidized to Co^{2+} in any location containing the cathode. Oxidation and dissolution of Co were not influenced by the Co/ionomer ratio in cracks and pores. Compared to Pt, the oxidation potential of Co was low. Thus, other than potential, the impact of the electrode catalyst structure, composition, particle diameter, and carbon was minor.

Same-View Nano-XAFS/STEM-EDS Maps After 10000 ADT-rec Cycles. Figure 7 shows the result of the same-view nano-XAFS/STEM-EDS of the MEA $\text{Pt}_3\text{Co}/\text{C}$ cathode after 10,000 ADT-rec cycles at 0.6–1.0 V. After 10,000 ADT-rec cycles, more cracks and pores formed in the cathode catalyst layer than the sample following the 5,000 ADT-rec cycles (Figure 7A), and the Pt and Co contents in the cracks and pores were less than in areas without dissolution (Figures 7B and 7C). Specifically, as shown in the EDS line profiles in Figure 1C and Figure 7C, ~90% of Co were dissolved and removed from the overall cathode layer, and ~1 % of Pt was dissolved as shown in Figure 1B and 7B. Furthermore, in the boundary area with the electrolytes, a Pt band was not observed after 5,000 ADT-rec cycles, indicating no occurrences of oxidation, dissolution, and reduction of Pt (Figures 7B and 7D). If we look at the Pt band closely, there was zerovalent Co (V_e in Figure 7E). Zerovalent Co is supported by the XANES spectrum of the cathode edge, shown in Figure 7H (region e), and based on the XANES spectrum we can see that it was more comparable to the Pt_3Co than Co foil (Figure 5B). Thus, there was overwhelmingly less Co than Pt, but this indicates that it formed a Pt_{100}Co alloy band. In addition, positively-charged Pt and Co were observed in the area between the Pt_{100}Co band and the cathode edge (v_e and V_e areas in Figures 7D and 7E, respectively). This state was similar to the distribution of Pt^{2+} in the area between the Pt band and the cathode edge in the deteriorated MEA Pt/C after 5,000 ADT-rec

cycles (Figure 4C). In the MEA Pt₃Co/C, after 10,000 ADT-rec cycles, there was oxidation of Pt in the cracks and pores of the cathode layer (Figure 7D). Co was largely dissolved from across the cathode electrocatalyst layer (~90%) and existed as Co²⁺ ions across the electrolytes (Figures 7C

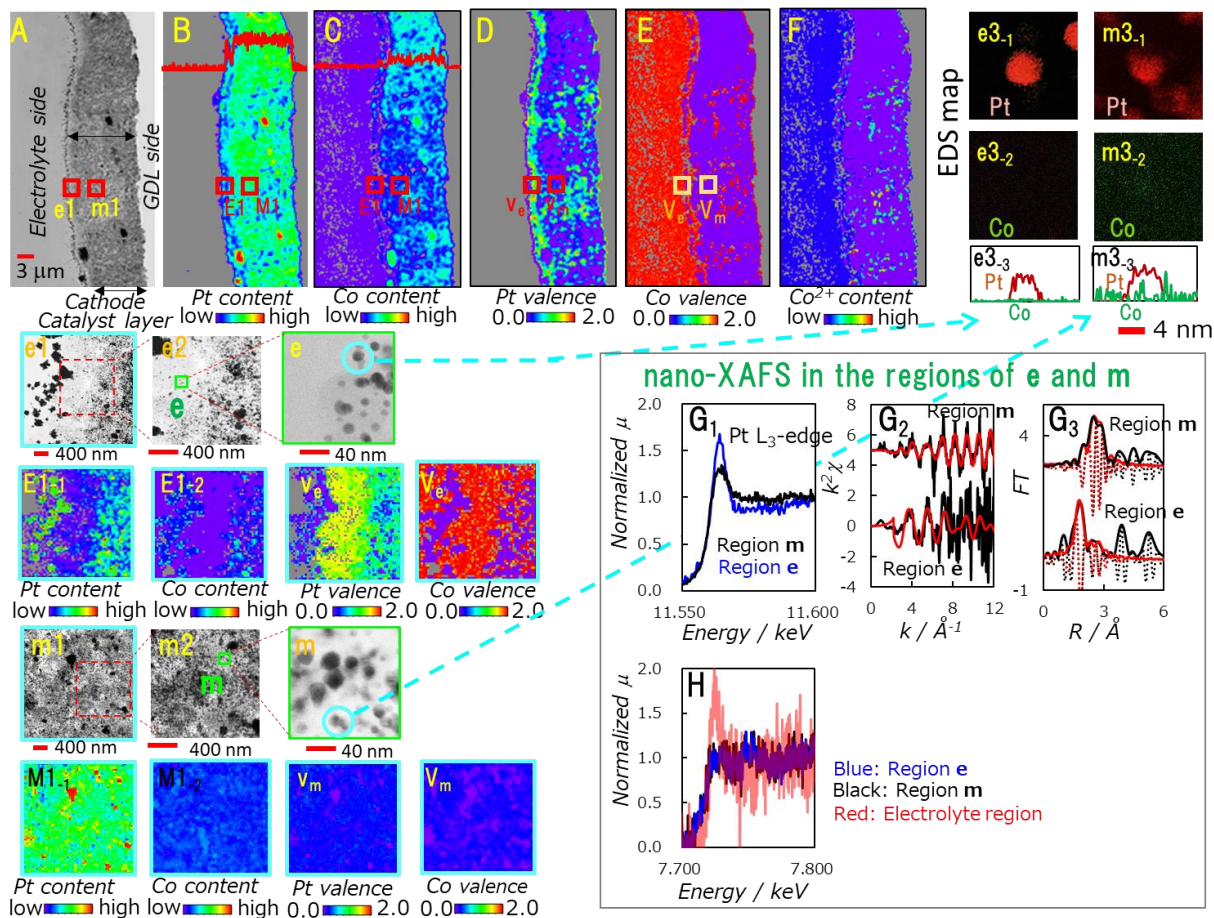


Figure 7. Results of nano-XAFS and STEM/EDS measurement of MEA Pt₃Co/C cathode electrocatalyst layer after 10,000 ADT-rec cycles. Nano-XAFS data: B-F, E1-1 & -2, v_e, V_e, M1-1 & -2, V_m, V_m, G₁-G₃, and H₁-H₃. STEM/EDS data: A, B(line profile), C(line profile), e1, e2, e, m1, m2, m, e3-1-3, and m3-1-3. A: STEM image, B: Pt content map and EDS line profile (decrease from Figure 2B), C: Co content map and EDS line profile (decrease from Figure 2C), D: Pt valence map, E: Co valence map, F: Co²⁺ content map (the same color bar in 7C). e1, E1, v_e and V_e: boundary region between the cathode electrocatalyst layer and electrolyte (3 mm x 3 mm). m1, M1, v_m and V_m: the middle region of the cathode electrocatalyst layer (3 mm x 3 mm). e3-1- e3-3: Pt EDS map, Co EDS map and Pt & Co line profiles for a single catalyst particle in the region **e**, respectively. m3-1- m3-3: Pt EDS map, Co EDS map and Pt & Co line profiles for a single catalyst particle in the region **m**, respectively. G₁- G₃: Pt L₃-edge XANES, EXAFS oscillations (black solid lines: observed; black dotted lines: imaginary part; red solid and dotted lines: curve fitted, respectively) and their associated Fourier transforms (black: observed; red: curve fitted) in the regions **e** (150 nm x 150 nm) and **m** (150 nm x 150 nm). H: Co K-edge XANES spectra in the regions **e** (blue; 150 nm x 150 nm) and **m** (black; 150 nm x 150 nm), and in the electrolyte region (red; 150 nm x 150 nm), respectively.

and 7E). In the sample after 10,000 ADT-rec cycles, and not only in the cathode catalyst layer, Co was dispersed across the wide region of the electrolytes, which, in turn, reduced Co concentration in each location. This prevented us from performing a Co K-edge nano-EXAFS analysis. However, Co^{2+} distributed in electrolytes likely exists as $[\text{Co}(\text{Nf}_{\text{sul}})_x(\text{H}_2\text{O})_y]^{2+}$ or $[\text{Co}(\text{H}_2\text{O})_6]^{2+}$ is similar to the result recorded after 5,000 ADT-rec cycles.

The Co content in the cathode layer was extremely low, and it is clear that it dissolved in areas other than the metallic nanoparticle cores. Although the Co content in the cathode electrocatalyst layer was low, zerovalent Co existed in the Pt-Co alloy core (V_m in Figure 7) and Co^{2+} ions in the cracks and pores of the cathode layer (Figures 7E and 7F). Table 1 shows the structural parameters obtained from the Pt L₃-edge EXAFS analysis of the area **m** in Figure 7e2 (150 nm × 150 nm). The $\text{CN}_{\text{Pt-Co}}$ was extremely small (0.1), and the Co/Pt ratio estimated from the comparison with $\text{CN}_{\text{Pt-Pt}}$ was 1/115. From the analysis of the Pt content (Figure 7E1.1) and the Co content (Figure 7E1.2) in the cathode edge area (3 μm × 3 μm), we discovered the existence of the metallic Pt-Co band in the electrolyte region of up to 300–400 nm from the cathode edge (E1.1, E1.2, v_e and V_e in Figure 7). In addition, in the area between the cathode edge and the Pt-Co band, though the amount was low, Pt (mean valence of 1.7+) and Co (2+) were observed (v_e and V_e in Figure 7). When the four-coordinated $\text{Pt}^{2+}\text{-O}_4$ species (probably square planar structure) are formed similar to the previous reports,⁵⁸⁻⁶⁰ the mole fraction of Pt^{2+} species calculated from Pt valence estimated from the nano-XANES (Figure 7G1) and the mole fraction of the $\text{Pt}^{2+}\text{-O}_4$ species calculated from $\text{CN}_{\text{Pt-O}}$ determined by EXAFS were 0.9 and 0.8, respectively, indicating that most Pt species existing the area between the cathode edge and the Pt-Co band are the $\text{Pt}^{2+}\text{-O}_4$ species. Pt^{2+} species also existed in the cracks and pores of the cathode layer (Figure 7D). Reduction in the Pt content associated with deterioration was small even after 10,000 ADT-rec cycles, but the rate of Co dissolution was high as above discussed, and was especially high (95%) in the area 300–600 nm from the boundary between the cathode and electrolytes.

Oxidation Number of Pt and Co, and the Distribution of Co^{2+} in the Depth Direction of the Cathode Catalyst. Figure 8 shows the oxidation state (valence) of Pt and Co and the distribution of Co^{2+} in the depth direction of the cathode electrocatalyst layer, i.e. the cathode layer from the boundary with the electrolyte to the boundary with GDL, during the MEA Pt₃Co/C degradation process. In the aging sample (before ADT-rec cycles), Pt valence was zero across the cathode

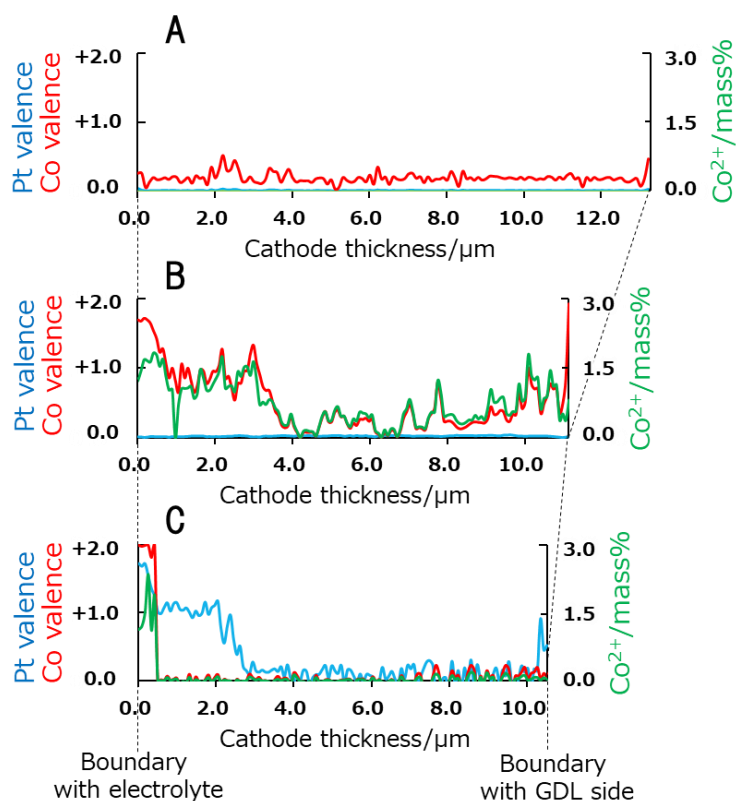


Figure 8. Distribution of Pt valence (light blue), Co valence (red), and Co^{2+} content (mass%) in the depth profiles in the MEA $\text{Pt}_3\text{Co}/\text{C}$ cathode electrocatalyst layers after aging (before ADT-rec) (A), after 5,000 ADT-rec cycles (B), and after 10,000 ADT-rec cycles (C).

electrocatalyst layer, while the Co valence was +0.2 (Figure 8A). As discussed above, considering Co^{2+} exists across the cathode layer after being oxidized and dissolved from the Pt_3Co nanoparticles in the aging process. 90% of Co atoms exist at zero-valence in the core of the core-shell type nanoparticles (Pt shell) (Figure 2 and Figure S5). After 5,000 ADT-rec cycles, the thickness of the cathode layer was reduced by 16% from 13.27 μm to 11.14 μm . Across the cathode catalyst layer, Pt was zerovalent. In contrast, valence of Co was the highest in the area near the boundary with the polymer electrolyte (mean valence: +1.7). Oxidation of Co was observed in the cathode range 4 μm from the boundary with the polymer electrolyte, and in the area of 4–8 μm , the amount of Co^{2+} did not increase, but there was a slight increase in the amount of Co^{2+} at 8 μm from the cathode edge on the GDL side (Figure 8B). Following 10,000 ADT-rec cycles, compared to after aging, the thickness of the cathode catalyst layer was reduced by 21% from 11.14 μm to 10.52 μm (Figure 8C). In addition, unlike after 5,000 ADT-rec cycles, there was an area of Pt

oxidation of up to 3 μm from the cathode edge; particularly, the mean valence of Pt was highest in the area 400 nm from the cathode edge (+1.7). After 10,000 ADT-rec cycles, $\sim 90\%$ of Co was dissolved and removed from the cathode layer, and a large number of Co^{2+} ions were observed in the area 400 nm from the boundary with the polymer electrolyte (Figure 8C). Co atoms that remained in the other areas of the cathode layer (other than cracks and pores) were limited to zerovalent Co atoms in the core of nanoparticles. As such, the chemical states of Pt and Co changed notably as a result of the 0.6–1.0 V rectangle wave ADT process in the area 4 μm from the boundary with the electrolytes, especially within 400 nm.

CONCLUSIONS

- (1) We have developed the same-view XAFS–STEM/EDS combination technique that is able to measure an MEA sample under atmospheric pressure with saturated water vapor pressure, while maintaining a PEFC operation environment as much as possible. Using this technique, we visualized and analyzed a chemical state map of the degradation process and the locations and factors of deterioration of the cathode catalyst of the MEA $\text{Pt}_3\text{Co}/\text{C}$ with 2.5 to 3 times more durability than the MEA Pt/C . As a result, we were able to observe the degradation process based on the suppression of oxidation and dissolution of Pt caused by Co in and out of catalyst particles not observed for the Pt/C .
- (2) The difference in the geometrical particle surface area and ECSA and the difference in catalyst particle sizes calculated from XRD and the catalyst diameter estimated from STEM, indicate that the surface of the Pt layer of the core-shell type $\text{Pt}_3\text{Co}/\text{C}$ was in disarray during the deterioration process.
- (3) The same-view nano-XAFS–STEM/EDS of the $150\text{ nm} \times 150\text{ nm}$ area revealed that in the cathode electrocatalyst layer of the aging MEA $\text{Pt}_3\text{Co}/\text{C}$, prior to the ADT-rec process, there were core-shell type nanoparticles forming from the core of intermetallic phase with $\text{Co}/\text{Pt}=1/2$ and two-layer Pt shells, and that after 5,000 ADT-rec cycles, the Co content in the cathode layer decreased approximately 70%, and the Pt shell layer increased to seven layers in the core-shell nanoparticles near the cathode edge and to four layers in the nanoparticles near the center of the cathode. In the MEA $\text{Pt}_3\text{Co}/\text{C}$ after 5,000 ADT-rec cycles, unlike the MEA Pt/C , no oxidation of Pt occurred anywhere in the cathode electrocatalyst layer, whereas Co with the

relatively lower oxidation potential was oxidized over a wide area of the cathode. Specifically, it was observed that there was a large quantity of Co^{2+} in the area from the boundary with the polymer electrolyte to about $\sim 4 \mu\text{m}$ inside the cathode.

- (4) In the MEA Pt/C, the larger the size and the smaller the Pt/ionomer ratio of the cracks and pores, the faster was the rate of dissolution of Pt. In contrast, in the MEA Pt₃Co/C, dissolution of Co was independent of the size of the cracks and pores or the Co/ionomer ratio. Co that was dissolved into the electrolytes had octahedral $\text{Co}^{2+}\text{-O}_6$ structures such as $[\text{Co}(\text{Nf}_{\text{sul}})_x(\text{H}_2\text{O})_y]^{2+}$ or $[\text{Co}(\text{H}_2\text{O})_6]^{2+}$ as Co^{2+} ions based on the same-view nano-EXAFS–STEM/EDS analysis of the $150 \text{ nm} \times 150 \text{ nm}$ area.
- (5) It is possible that the MEA Pt₃Co/C after 5,000 ADT-rec cycles had a four-to-seven-layer Pt shell structure and the same properties as the bulk Pt, leading to oxidation and dissolution observed with the MEA Pt/C. However, oxidation and dissolution of Pt was suppressed. The reason for this is that $[\text{Co}(\text{Nf}_{\text{sul}})_x(\text{H}_2\text{O})_y]^{2+}$ or $[\text{Co}(\text{H}_2\text{O})_6]^{2+}$ adsorbed on the Pt shell surface, thereby suppressing the oxidation of Pt to Pt^{2+} . Alternatively, effective concentrations of Nf_{sul} and $\text{Nf}_{\text{sulf}^-}$ of Nafion ionomers near the cathode edge and in the cracks and pores were reduced by coordination to Co^{2+} ions, resulting in suppression of Pt^{2+} dissolution.
- (6) After 10,000 ADT-rec cycles, many cracks and pores formed in the cathode catalyst layer, and about 90% of Co was dissolved and removed from the cathode layer. The rate of Co dissolution at the cathode was especially high (95%) for the boundary area with the polymer electrolyte (300–600 nm).
- (7) In the MEA Pt₃Co/C after 10,000 ADT-rec cycles, there was a metallic Pt-Co alloy band in the electrolyte region approximately 300–400 nm from the cathode edge. The same-view nano-XAFS–STEM/EDS combination technique in the $150 \text{ nm} \times 150 \text{ nm}$ area identified 4-coordinated $\text{Pt}^{2+}\text{-O}_4$ species and 6-coordinated $\text{Co}^{2+}\text{-O}_6$ species in the area between the cathode edge and the Pt-Co band. Oxidation of Pt was also observed in the cracks and pores of the cathode layer.

EXPERIMENTAL SECTION

MEA Samples. We used Pt₃Co/C (TEC36E52; 46.5 wt% Pt, 4.5 wt% Co) and Pt/C(TEC10E50E; 50 wt% Pt) from Tanaka Kikinzoku Kogyo as the cathode catalyst of MEA and as a reference

sample, respectively. We mixed ionomer (EW1100) with these materials so that the Pt/ionomer ratio was 1/1. The coating area of the catalyst was 3 cm × 3 cm, and the metal loading was 0.3 mg_{Pt}/cm². We used Nafion-212 as the proton-exchange membrane (8 cm × 8 cm). In the present study, we examined the MEA following the aging (conditioning) processes, and samples after 5,000 and 10,000 rectangle accelerated durability test (ADT-rec) cycles at 0.6 V (3 s)–1.0 V (3 s).

Electrochemical Measurements. PEFC cell temperature, humidifier temperature, and gas line temperature were maintained at 80 °C, 78 °C (provides 92% cell relative humidity), and 95 °C, respectively. Before performing the electrochemical measurements, the MEAs were conditioned (aging process) by applying 150 polarization cycles consisting of the galvanostatic steps (6 s step duration) between 0.002 A cm⁻² (near open circuit voltage) and 0.5 A cm⁻² under a H₂ flow of 165 sccm at anode and an air flow of 900 sccm at cathode. After the MEA aging, 4 cycles of cyclic voltammograms (CV) were measured between 0.05 V and 0.9 V (vs RHE) by applying 50 and 20 mV s⁻¹ potential scan speeds, respectively, and the final cycle of the CV measured at 20 mV s⁻¹ was used to determine the electrochemical surface area (ECSA) under a H₂ flow of 165 sccm at anode and a N₂ flow of 200 sccm at cathode. I-V load measurements were performed under a H₂ flow of 165 sccm at the anode, and an air flow of 1,320 sccm at the cathode. The rectangle ADT process was performed with 0.6 V (3 s)–1.0 V (3 s) cyclic treatments under a H₂ flow of 165 sccm at the anode and a N₂ flow of 200 sccm at the cathode. ECSA was obtained from the hydrogen desorption current in CV at 0.05–0.35 V.

Same-View Measurement of Nano-XAFS/STEM-EDS. After completing all electrochemical measurements, we returned the atmosphere to N₂ flow, confirmed that OCV had been sufficiently reduced, then removed the MEA from the cell, using a glove bag at N₂ atmospheric pressure with saturation water vapor pressure. After removing the MEA, a small piece was cutted out of the MEA and embedded in epoxy resin, and a thin section with a thickness of 200 nm was prepared with ultramicrotome. We placed this sample on a SiN membrane so that the cross-section of the MEA (depth direction) faced upwards. After surrounding this sample with a 300-nm gasket tube spacer, another SiN membrane was assigned, then the sample was sealed with epoxy resin (Figure S6). All operations were performed under humid N₂ atmosphere to prevent vaporization of water from the sample and oxidation of the MEA electrode catalyst. During these operations, the MEA Pt₃Co/C scarcely changed, and the degradation process was slow; thus, the result of the *ex situ*

same-view measurement can be assumed to be equivalent to the projected measurement result of an *in situ* sample.^{24,65}

We measured the STEM-EDS of a $80\ \mu\text{m} \times 30\ \mu\text{m}$ area of an MEA thin section sample fixed in a SiN membrane stacking cell (Figure S6). Measurement temperature was controlled at $25\ ^\circ\text{C}$, at which there was no evaporation of water or reduction in fluorine due to an electron beam in the SiN membrane stacking cell. The mean particle diameter of the cathode catalyst was obtained from more than 300 particles from the central area of the cathode layer, the boundary area between the cathode layer and the polymer electrolyte membrane, and the boundary area between the cathode layer and the gas diffusion layer (GDL). We obtained the ionomer distribution of the MEA from the EDS count of F element. An analysis of the core-shell structure of the catalyst nanoparticles was performed by averaging the number of atomic layers in the shell layers, comprised of 10 to 20 particles, and the core structure.

Nano-XAFS Measurement. We performed nano-XAFS measurements of a thin section of MEA fixed in the SiN membrane stacking cell with the same view as the location of the STEM/EDS measurement, using the same method as in the previous report,⁵⁸⁻⁶⁰ by means of a focused beam of $150\ \text{nm} \times 150\ \text{nm}$ (Figure S6). For the nano-XANES map, we measured a wide area of approximately $80\ \mu\text{m} \times 30\ \mu\text{m}$ and a narrow area of $8\ \mu\text{m} \times 8\ \mu\text{m}$, including the cathode electrocatalyst layer. The Pt L₃-edge and Co K-edge nano-XAFS spectra were measured at BL36XU in SPring-8 by using a Si(111) double-crystal monochromator. X-ray beam was focused to $150\ \text{nm} \times 150\ \text{nm}$ size via a pair of elliptically bent Kirkpatrick-Baez (KB) mirrors. The nano-XAFS spectra were measured in a fluorescence mode with Vortex-ME IV detector, where the sample was inclined to the X-ray nanobeam by 30° . Nano-XANES maps were obtained by scanning nano-XAFS methods,⁵⁷⁻⁶⁰ where XAFS spectra were measured at 206 and 136 energy points for the energy range of 11.390 to 12.200 keV and 7.520 to 7.810 keV for Pt L₃-edge and Co K-edge XANES, respectively. In order to avoid a sample damage from the X-ray beam irradiation, the beam stay time in a pixel point was shortened as much as possible. Nano-XAFS mapping was performed for 1–2 views of about $65\ \mu\text{m} \times 30\ \mu\text{m}$ and 1 view of $3\ \mu\text{m} \times 14\ \mu\text{m}$ using nano-X-ray beam with $150\ \text{nm} \times 150\ \text{nm}$ size every 400 and 100 nm steps, respectively. Beam stay time at the same nanoposition for nano-XAFS maps in about both $65\ \mu\text{m} \times 30\ \mu\text{m}$ and $3\ \mu\text{m} \times 4\ \mu\text{m}$ regions was only 5 and 30 ms for Pt L₃-edge and Co K-edge, respectively.

Nano-EXAFS measurements were also performed in $150 \text{ nm} \times 150 \text{ nm}$ regions with $60 \text{ s} \times$ loops and $300 \text{ s} \times 10$ loops measurements for Pt L₃-edge and Co K-edge, respectively. The measurement ranges are 11.450 to 12.900 keV and 7.650 to 8.200 keV for Pt L₃-edge and Co K-edge, respectively.

After the nano-XAFS measurements, we measured STEM-EDS of the same area as the one measured for nano-XAFS. Furthermore, we performed particle analysis of the characteristic area observed on the nano-XANES map, via STEM-EDS.

Positional correction. Positional correction in the same-view measurement was performed using the same method as in the report.⁵⁸ The amount of Pt and Co was obtained from 11.600 keV or 7.760 keV of the arctangent function, calculated from the linear combination fitting of the Lorentzian function and the arctangent function in the XANES spectrum (Pt: 11.550–11.600 keV, Co: 7.700–7.800 keV). Valence of Pt was obtained from an approximation equation obtained through linear fitting of the white line peak area for Pt⁰ foil, PtO, and PtO₂ reference samples by using the area of the Lorentzian function from the above analysis as the white line peak area.^{31,32,34} Since Co K-edge XANES and EXAFS for Co species, which were dissolved into the polymer electrolyte membrane, were consistent with those of [Co(H₂O)₆]²⁺ (Figure S3), valence of Co was obtained from the compositional ratio of the XANES spectrum of the sample via linear combination analysis of Pt₃Co alloy (Pt₃Co alloy plate, TKK) and [Co(H₂O)₆]²⁺.

XAFS Data Analysis. EXAFS Fourier-transform fittings were performed similar to the previous reports,⁶⁵ using the data analysis program IFEFFIT (version 1.2.11c).⁶⁶ Theoretical phase shift and backscattering amplitude functions were calculated by FEFF 8.20.⁶⁷ Normalized white-line peak areas for the estimation of Pt valences were calculated by using Lorentzian and Arctangent functions by IFEFFIT. We used s_0^2 values of 0.88, 0.90, 0.90, 0.90, and 0.88 in the determination of CN(Pt–Pt), CN(Pt–O), CN(Co–Pt), CN(Co–Co), and CN(Co–O), respectively. The Fourier transform range taken in the $k^2\chi$ plots and the curve-fitting range in R space were 3–11 Å⁻¹ and 1.4–3.2 Å, respectively. To avoid divergence in the XANES fitting analysis of the XANES mapping regions, we ignored regions with low Pt and Co contents below 1/100 of $\mu_{11.600 \text{ keV}}$ and $\mu_{7.800 \text{ keV}}$, respectively.

ASSOCIATED CONTENT

Supporting Information. The Supporting Information is available free of charge on the ACS Publications website. Same-view membrane cell; CV; ECSA; I-V curves; XRD; nano-XANES spectra; nano-EXAFS data analysis; STEM/EDS (PDF)

AUTHOR INFORMATION

Corresponding Author

*E-mail: iwasawa@pc.uec.ac.jp. Phone: +81-42-443-5921. Fax: +81-42-443-5483.

ORCID

Yasuhiro Iwasawa: 0000-0002-5222-5418

Author Contributions

The manuscript was written through contributions of all authors. All authors have given approval to the final version of the manuscript.

Funding Sources

The New Energy and Industrial Technology Development Organization (NEDO) PEFC Program.

Notes

The authors declare no competing financial interest.

ACKNOWLEDGMENTS

This work was supported by the New Energy and Industrial Technology Development Organization (NEDO). XAFS measurements were performed with the approval of SPring-8 subject numbers 2016A7804, 2016B7804, and 2017A7804, 2017A7807, 2017B7804, 2018A7804, 2018B7804, and 2019A7804.

REFERENCES

1. Seh, Z. W.; Kibsgaard, J.; Dickens, C. F.; Chorkendorff, I.; Nørskov, J. K.; Jaramillo, T. F. Combining Theory and Experiment in Electrocatalysis: Insights into Materials Design, *Science* **2017**, *355*, 6321, eaad4998, 1-33.
2. Stephens, I. E. L.; Rossmeisl, J.; Chorkendorff, I. Toward Sustainable Fuel cells, *Science*, **2016**, *354*, 1378-1379.
3. Debe, M. K. Electrocatalyst Approaches and Challenges for Automotive Fuel Cells, *Nature*, **2012**, *486*, 43-51.
4. Li, J.; Yin, H.-M.; Li, X.-B.; Okunishi, E.; Shen, Y.-L.; He, J.; Tang, Z.-K.; Wang, W.-X.; Yücelen, E.; Li, C.; Gong, Y.; Gu, L.; Miao, S.; Liu, L.-M.; Luo, J.; Ding, Y. Surface Evolution of a Pt-Pd-Au Electrocatalyst for Stable Oxygen Reduction, *Nat. Energy* **2017**, *2*, 17111-1-9.
5. Bu, L.; Zhang, N.; Guo, S.; Zhang, X.; Li, J.; Yao, J.; Wu, T.; Lu, G.; Ma, J.-Y.; Su, D.; Huang, X. Biaxially Strained PtPb/Pt Core/shell Nanoplate Boosts Oxygen Reduction Catalysis, *Science* **2016**, *354*, 1410-1414.
6. Stamenkovic, V. R.; Mun, B. S.; Arenz, M.; Mayrhofer, K. J. J.; Lucas, C. A.; Wang, G.; Ross, P. N.; Markovic, N. M. Trends in Electrocatalysis on Extended and Nanoscale Pt-Bimetallic Alloy surfaces, *Nat. Mater.* **2007**, *6*, 241-247.
7. Beermann, V.; Gocyla, M.; Köhl, S.; Padgett, E.; Schmies, H.; Goerlin, M.; Erini, N.; Shviro, M.; Heggen, M.; Dunin-Borkowski, R. E.; Müller, D. A.; Strasser, P. Tuning the Electrocatalytic Oxygen Reduction Reaction Activity and Stability of Shape-Controlled Pt-Ni Nanoparticles by Thermal Annealing-Elucidating the Surface Atomic Structural and Compositional Changes, *J. Am. Chem. Soc.* **2017**, *139*, 16536-16547.
8. Li, M. F.; Zhao, Z. P.; Cheng, T.; Fortunelli, A.; Chen, C. Y.; Yu, R.; Zhang, Q. H.; Gu, L.; Merinov, B. V.; Li, Z. Y.; Zhu, E. B.; Yu, T.; Jia, Q. Y.; Guo, J. H.; Zhang, L.; Goddard, W. A.; Huang, Y.; Duan, X. F. Ultrafine Jagged Platinum Nanowires Enable Ultrahigh Mass Activity for the Oxygen Reduction Reaction, *Science* **2016**, *354*, 1414-1419.
9. Escudero-Escribano, M.; Malacrida, P.; Hansen, M. H.; Vej-Hansen, U. G.; Velázquez-Palenzuela, A.; Tripkovic, V.; Schiøtz, J.; Rossmeisl, J.; Stephens, I. E. L.; Chorkendorff, I. Tuning the Activity of Pt Alloy Electrocatalysts by Means of the Lanthanide Contraction, *Science* **2016**, *352*, 73-76.

10. Li, J.; Alsudairi, A.; Ma, Z.-F.; Mukerjee, S.; Jia, Q. Asymmetric Volcano Trend in Oxygen Reduction Activity of Pt and Non-Pt Catalysts: In Situ Identification of the Site-Blocking Effect, *J. Am. Chem. Soc.* **2017**, *139*, 1384-1387.
11. Huang, X.; Zhao, Z.; Cao, L.; Chen, Y.; Zhu, E.; Lin, Z.; Li, M.; Yan, A.; Zettl, A.; Wang, Y. M.; Duan, X.; Mueller, T.; Huang, Y. High-Performance Transition Metal-Doped Pt₃Ni Octahedra for Oxygen Reduction Reaction, *Science* **2015**, *348*, 1230-1234.
12. Zhang, L.; Roling, L. T.; Wang, X.; Vara, M.; Chi, M.; Liu, J.; Choi, S.-I.; Park, J.; Herron, J. A.; Xie, Z.; Mavrikakis, M.; Xia, Y. Platinum-Based Nanocages with Subnanometer-Thick Walls and Well-Defined, Controllable Facets, *Science* **2015**, *349*, 412-416.
13. Shao, M.; Chang, Q.; Dodelet, J.-P.; Chenitz, R. Recent Advances in Electrocatalysts for Oxygen Reduction Reaction, *Chem. Rev.* **2016**, *116*, 3594-3657.
14. Stamenkovic, V.; Mun, B. S.; Mayrhofer, K. J. J.; Ross, P. N.; Markovic, N. M.; Rossmeisl, J.; Greeley, J.; Nørskov, J. K. Changing the Activity of Electrocatalysts for Oxygen Reduction by Tuning the Surface Electronic Structure, *Angew. Chem. Int. Ed.* **2006**, *45*, 2897-2901.
15. Cui, C.; Gan, L.; Heggen, M.; Rudi, S.; Strasser, P. Compositional Segregation in shaped Pt Alloy Nanoparticles and Their Structural Behaviour during Electrocatalysis, *Nat. Mater.* **2013**, *12*, 765-771.
16. Wang, D.; Xin, H. L.; Hovden, R.; Wang, H.; Yu, Y.; Muller, D. A.; DiSalvo, F. J.; Abruña, H. D. Structurally Ordered Intermetallic Platinum-Cobalt Core-Shell Nanoparticles with Enhanced Activity and Stability as Oxygen Reduction Electrocatalysts, *Nat. Mater.* **2013**, *12*, 81-87.
17. Zhang, J.; Sasaki, K.; Sutter, E.; Adzic, R. R. Stabilization of Platinum Oxygen-Reduction Electrocatalysts Using Gold Clusters, *Science* **2007**, *315*, 220-222.
18. Chen, C.; Kang, Y.; Huo, Z.; Zhu, Z.; Huang, W.; Xin, H. L.; Snyder, J. D.; Li, D.; Herron, J. A.; Mavrikakis, M.; Chi, M.; More, K. L.; Li, Y.; Markovic, N. M.; Somorjai, G. A.; Yang, P.; Stamenkovic, V. R. Highly Crystalline Multimetallic Nanoframes with Three-Dimensional Electrocatalytic Surfaces, *Science* **2014**, *343*, 1339-1343.
19. Stamenkovic, V. R.; Fowler, B.; Mun, B. S.; Wang, G. F.; Ross, P. N.; Lucas, C. A.; Markovic, N. M. Improved Oxygen Reduction Activity on Pt₃Ni(111) via Increased Surface Site Availability, *Science* **2007**, *315*, 493-497.

20. Chen, S.; Ferreira, P. J.; Sheng, W. C.; Yabuuchi, N.; Allard, L. F.; Shao-Horn, Y. Enhanced Activity for Oxygen Reduction Reaction on “Pt₃Co” Nanoparticles: Direct Evidence of Percolated and Sandwich-Segregation Structure, *J. Am. Chem. Soc.* **2008**, *130*, 13818-13819.
21. Zhao, X.; Takao, S.; Higashi, K.; Kaneko, T.; Samjeskè, G.; Sekizawa, O.; Sakata, T.; Yoshida, Y.; Uruga, T.; Iwasawa, Y. Simultaneous Improvements in Performance and Durability of an Octahedral PtNi_x/C Electrocatalyst for Next-Generation Fuel Cells by Continuous, Compressive, and Concave Pt Skin Layers, *ACS Catal.* **2017**, *7*, 4642-4654.
22. Nagasawa, K.; Takao, S.; Nagamatsu, S.; Samjeské, G.; Sekizawa, O.; Kaneko, T.; Higashi, K.; Yamamoto, T.; Uruga, T.; Iwasawa, Y. Surface-Regulated Nano-SnO₂/Pt₃Co/C Cathode Catalysts for Polymer Electrolyte Fuel Cells Fabricated by a Selective Electrochemical Sn Deposition Method, *J. Am. Chem. Soc.* **2015**, *137*, 12856-12864.
23. Tada, M.; Uruga, T.; Iwasawa, Y. Key Factors Affecting the Performance and Durability of Cathode Electrocatalysts in Polymer Electrolyte Fuel Cells Characterized by In Situ Real Time and Spatially Resolved XAFS Techniques, *Catal. Lett.* **2015**, *145*, 58-70.
24. Tada, M.; Iwasawa, Y. “Fuel Cells by Advanced XAFS Techniques” in “XAFS Techniques for Catalysts, Nanomaterials, and Surfaces” (Iwasawa, Y., Asakura, K., Tada, M., Eds.), Springer, **2017**, 335-349.
25. Casalongue, H. S.; Kaya, S.; Viswanathan, V.; Miller, D. J.; Friebe, D.; Hansen, H. A.; Nørskov, J. K.; Nilsson, A.; Ogasawara, H. Direct Observation of the Oxygenated Species during Oxygen Reduction on a Platinum Fuel Cell Cathode, *Nat. Comm.* **2013**, *4*, 2817-1-6.
26. Uruga, T.; Tada, M.; Sekizawa, O.; Takagi, Y.; Yokoyama, T.; Iwasawa, Y. SPring-8 BL36XU: Synchrotron Radiation X-ray-Based Multi-Analytical Beamline for Polymer Electrolyte Fuel Cells under Operating Conditions, *Chem. Rec.* **2019**, *19*, 1444-1456.
27. Tada, M.; Murata, S.; Asakoka, T.; Hiroshima, K.; Okumura, K.; Tanida, H.; Uruga, T.; Nakanishi, H.; Matsumoto, S.; Inada, Y.; Nomura, M.; Iwasawa, Y. In Situ Time-Resolved Dynamic Surface Events on the Pt/C Cathode in a Fuel Cell under Operando Conditions, *Angew. Chem. Int. Ed.* **2007**, *46*, 4310-4315.
28. Ishiguro, N.; Saida, T.; Uruga, T.; Nagamatsu, S.; Sekizawa, O.; Nitta, K.; Yamamoto, T.; Ohkoshi, S.; Iwasawa, Y.; Yokoyama, T.; Tada, M. Operando Time-Resolved X-ray Absorption Fine Structure Study for Surface Events on a Pt₃Co/C Cathode Catalyst in a Polymer Electrolyte Fuel Cell during Voltage-Operating Processes, *ACS Catal.* **2012**, *2*, 1319-1330.

29. Ishiguro, N.; Saida, T.; Uruga, T.; Sekizawa, O.; Nagasawa, K.; Nitta, K.; Yamamoto, T.; Ohkoshi, S.; Yokoyama, T.; Tada, M. Structural Kinetics of a Pt/C Cathode Catalyst with Practical Catalyst Loading in an MEA for PEFC Operating Conditions Studied by in situ Time-Resolved XAFS, *Phys. Chem. Chem. Phys.* **2013**, *15*, 18827-18834.
30. Ishiguro, N.; Uruga, T.; Sekizawa, O.; Tsuji, T.; Suzuki, M.; Kawamura, N.; Mizumaki, M.; Nitta, K.; Yokoyama, T.; Tada, M. Visualization of the Heterogeneity of Cerium Oxidation States in Single Pt/Ce₂Zr₂O_x Catalyst Particles by Nano-XAFS, *ChemPhysChem*, **2014**, *15*, 1563-1568.
31. Nagamatsu, S.; Arai, T.; Yamamoto, M.; Ohkura, T.; Oyanagi, H.; Ishizaka, T.; Kawanami, H.; Uruga, T.; Tada, M.; Iwasawa, Y. Potential-Dependent Restructuring and Hysteresis in the Structural and Electronic Transformations of Pt/C, Au(Core)-Pt(Shell)/C, and Pd(Core)-Pt(Shell)/C Cathode Catalysts in Polymer Electrolyte Fuel Cells Characterized by in Situ X-ray Absorption Fine Structure, *J. Phys. Chem. C* **2013**, *117*, 13094-13107.
32. Nagamatsu, S.; Takao, S.; Samjeské, G.; Nagasawa, K.; Sekizawa, O.; Kaneko, T.; Higashi, K.; Uruga, T.; Gayen, S.; Velaga, S.; Saniyal, M. K.; Iwasawa, Y. Structural and Electronic Transformations of Pt/C, Pd@Pt(1 ML)/C and Pd@Pt(2 ML)/C Cathode Catalysts in Polymer Electrolyte Fuel Cells during Potential-Step Operating Processes Characterized by In-situ Time-Resolved XAFS, *Surf. Sci.*, **2016**, *648*, 100-113.
33. Ishiguro, N.; Kityakarn, S.; Sekizawa, O.; Uruga, T.; Matsui, H.; Taguchi, M.; Nagasawa, K.; Yokoyama, T.; Tada, M. Kinetics and Mechanism of Redox Processes of Pt/C and Pt₃Co/C Cathode Electrocatalysts in a Polymer Electrolyte Fuel Cell during an Accelerated Durability Test, *J. Phys. Chem. C*, **2016**, *120*, 19642-19651.
34. Kaneko, T.; Samjeské, G.; Nagamatsu, S.; Higashi, K.; Sekizawa, O.; Takao, S.; Yamamoto, T.; Zhao, X.; Sakata, T.; Uruga, T.; Iwasawa, Y. Key Structural Kinetics for Carbon Effects on the Performance and Durability of Pt/Carbon Cathode Catalysts in Polymer Electrolyte Fuel Cells Characterized by In Situ Time-Resolved X-ray Absorption Fine Structure, *J. Phys. Chem. C*, **2016**, *120*, 24250-24264.
35. Higashi, K.; Samjeské, G.; Takao, S.; Kaneko, T.; Sekizawa, O.; Uruga, T.; Iwasawa, Y. The Relationship between the Active Pt Fraction in a PEFC Pt/C Catalyst and the ECSA and Mass Activity during Start-Up/Shut-Down Degradation by in Situ Time-Resolved XAFS Technique, *J. Phys. Chem. C* **2017**, *121*, 22164-22177.

36. Sekizawa, O.; Uruga, T.; Higashi, K.; Kaneko, T.; Yoshida, Y.; Sakata, T.; Iwasawa, Y. Simultaneous Operando Time-Resolved XAFS–XRD Measurements of a Pt/C Cathode Catalyst in Polymer Electrolyte Fuel Cell under Transient Potential Operations, *ACS Sus. Chem. Eng.*, **2017**, *5*, 3631-3636.
37. Sekizawa, O.; Kaneko, T.; Higashi, K.; Takao, S.; Yoshida, Y.; Gunji, T.; Zhao, X.; Samjeské, G.; Sakata, T.; Uruga, T.; Iwasawa, Y. Key Structural Transformations and Kinetics of Pt Nanoparticles in PEFC Pt/C Electrocatalysts by a Simultaneous Operando Time-Resolved QXAFS-XRD Technique, *Top. Catal.* **2018**, *61*, 889-901.
38. Ishiguro N.; Tada, M. Structural Kinetics of Cathode Events on Polymer Electrolyte Fuel Cell Catalysts Studied by Operando Time-Resolved XAFS, *Catal. Lett.* **2018**, *148*, 1597-1609.
39. Ozawa, S.; Matsui, H.; Ishiguro, N.; Tan, Y.; Maejima, N.; Taguchi, M.; Uruga, T.; Sekizawa, O.; Nagasawa, K.; Higashi, K.; Tada, M. Operando Time-Resolved X-ray Absorption Fine Structure Study for Pt Oxidation Kinetics on Pt/C and Pt₃Co/C Cathode Catalysts by Polymer Electrolyte Fuel Cell Voltage Operation Synchronized with Rapid O₂ Exposure, *J. Phys. Chem.* **2018**, *C 122*, 14511-14517.
40. Saida, T.; Sekizawa, O.; Ishiguro, N.; Hoshino, M.; Uesugi, K.; Uruga, T.; Ohkoshi, S.; Yokoyama, T.; Tada, M. 4D Visualization of a Cathode Catalyst Layer in a Polymer Electrolyte Fuel Cell by 3D Laminography-XAFS, *Angew. Chem. Int. Ed.* **2012**, *51*, 10311-10314.
41. Matsui, H.; Ishiguro, N.; Enomoto, K.; Sekizawa, O.; Uruga, T.; Tada, M. Imaging of Oxygen Diffusion in Individual Platinum/Ce₂Zr₂O_x Catalyst Particles During Oxygen Storage and Release, *Angew. Chem. Int. Ed.*, **2016**, *55*, 12022-12025.
42. Matsui, H.; Ishiguro, N.; Uruga, T.; Sekizawa, O.; Higashi, K.; Maejima, N.; Tada, M. Operando 3D Visualization of Migration and Degradation of a Platinum Cathode Catalyst in a Polymer Electrolyte Fuel Cell, *Angew. Chem. Int. Ed.* **2017**, *56*, 9371-9375.
43. Sekizawa, O.; Uruga, T.; Ishiguro, N.; Matsui, H.; Higashi, K.; Sakata, T.; Iwasawa, Y.; Tada, M. In-situ X-ray nano-CT System for Polymer Electrolyte Fuel Cells under Operating Conditions, *J. Phys.: Conf. Series* **2017**, *849*, 012022-1-4.
44. Higashi, K.; Sakata, T.; Sekizawa, O.; Ishiguro, N.; Samjeské, G.; Takao, S.; Kaneko, T.; Uruga, T.; Iwasawa, Y.; Tada, M. In-situ 3D CT-XAFS Imaging of Pt/C Cathode Catalysts in Polymer Electrolyte Fuel Cell during Degradation Processes by Anode Gas Exchange Cycles, *Microsc. Microanal.* **2018**, *24 (S2)*, 442-443.

45. Tan, Y.; Matsui, H.; Ishiguro, N.; Tada, M. Three-Dimensional XAFS Imaging of Polymer Electrolyte Fuel Cell Cathode Catalysts in Membrane Electrode Assembly, *Acc. Mater. Surf. Res.* **2018**, *3*, 165-171.
46. Matsui, H.; Maejima, N.; Ishiguro, N.; Tan, Y.; Uruga, T.; Sekizawa, O.; Sakata, T.; Tada, M. Operando XAFS Imaging of Distribution of Pt Cathode Catalysts in PEFC MEA, *Chem. Rec.* **2019**, *19*, 1380-1392.
47. Buurmans I. L. C.; Weckhuysen, B. M. Heterogeneities of Individual Catalyst Particles in Space and Time as Monitored by Spectroscopy, *Nat. Chem.* **2012**, *4*, 873-886.
48. Vogt, C.; Groeneveld, E.; Kamsma, G.; Nachtegaal, M.; Lu, L.; Kiely, C. J.; Berben, P. H.; Meirer, F.; Weckhuysen, B. M. Unravelling Structure Sensitivity in CO₂ Hydrogenation Over Nickel, *Nat. Catal.* **2018**, *1*, 127-134.
49. Karim, W.; Spreafico, C.; Kleibert, A.; Gobrecht, J.; Vondele, J. V.; Ekinici, Y.; Bokhoven, J. A. Catalyst Support Effects on Hydrogen Spillover, *Nature*, **2017**, *541*, 68-71.
50. Ebner, M.; Marone, F.; Stampanoni, M.; Wood, V. Visualization and Quantification of Electrochemical and Mechanical Degradation in Li Ion Batteries, *Science*, **2013**, *342*, 716-720.
51. Berejnova, V.; Saha, M. S.; Susaca, D.; Stumpera, J.; Westb, M. M.; Hitchcock, A. P. Advances in Structural Characterization Using Soft X-ray Scanning Transmission Microscopy (STXM): Mapping and Measuring Porosity in PEM-FC Catalyst Layers, *ECS Transactions*, **2017**, *80*, 241-252.
52. Beyerlein, K. R. Time-Spliced X-ray Diffraction Imaging of Magnetism Dynamics in a NdNiO₃ Thin Film, *Proc. Natl. Acad. Sci.* **2018**, *115*, 2044-2048.
53. Cornelius, T. W.; Thomas, O. Progress of *in situ* Synchrotron X-ray Diffraction Studies on the Mechanical Behavior of Materials at Small Scales, *Prog. Mater. Sci.* **2018**, *94*, 383-434.
54. Mara, M. W.; Hadt, R. G.; Reinhard, M. E.; Kroll, T.; Lim, H.; Hartsock, R. W.; Mori, R. A.; Chollet, M.; Glowacki, J. M.; Nelson, S.; Sokaras, D.; Kunnus, K.; Hodgson, K. O.; Hedman, B.; Bergmann, U.; Gaffney, K. J.; Solomon, E. I. Metalloprotein Entatic Control of Ligand-Metal Bonds Quantified by Ultrafast X-ray Spectroscopy, *Science*, **2017**, *356*, 1276-1280.
55. Hirose, M.; Ishiguro, N.; Shimomura, K.; Burdet, N.; Matsui, H.; Tada, M.; Takahashi, Y. Visualization of Heterogeneous Oxygen Storage Behavior in Platinum-Supported Cerium-Zirconium Oxide Three-Way Catalyst Particles by Hard X-ray Spectro-Ptychography, *Angew. Chem. Int. Ed.* **2018**, *57*, 1474-1479.

56. Schmidt, J. E.; Oord, R.; Guo, W.; Poplawsky, J. D.; Weckhuysen, B. M. Nanoscale Tomography Reveals the Deactivation of Automotive Copper-Exchanged Zeolite Catalysts, *Nat. Commun.* **2017**, *8*, 1666-1-8.
57. Takao, S.; Sekizawa, O.; Nagamatsu, S.; Kaneko, T.; Yamamoto, T.; Samjeské, G.; Higashi, K.; Nagasawa, K.; Tsuji, T.; Suzuki, M.; Kawamura, N.; Mizumaki, M.; Uruga, T.; Iwasawa, Y. Mapping Platinum Species in Polymer Electrolyte Fuel Cells by Spatially Resolved XAFS Techniques, *Angew. Chem. Int. Ed.* **2014**, *53*, 14110-14114.
58. Takao, S.; Sekizawa, O.; Samjeské, G.; Nagamatsu, S.; Kaneko, T.; Yamamoto, T.; Higashi, K.; Nagasawa, K.; Uruga, T.; Iwasawa, Y. Same-View Nano-XAFS/STEM-EDS Imagings of Pt Chemical Species in Pt/C Cathode Catalyst Layers of a Polymer Electrolyte Fuel Cell, *J. Phys. Chem. Lett.* **2015**, *6*, 2121-2126.
59. Takao, S.; Sekizawa, O.; Samjeské, G.; Nagamatsu, S.; Kaneko, T.; Higashi, K.; Yamamoto, T.; Nagasawa, X.; K.; Uruga, T.; Iwasawa, Y. Spatially Non-Uniform Degradation of Pt/C Cathode Catalysts in Polymer Electrolyte Fuel Cells Imaged by Combination of Nano XAFS and STEM-EDS Techniques, *Top. Catal.* **2016**, *59*, 1722-1731.
60. Takao, S.; Sekizawa, O.; Samjeské, G.; Kaneko, T.; Higashi, K.; Yoshida, Y.; Skata, T.; Yamamoto, Gunji, T.; Uruga, T.; Iwasawa, Y. Observation of Degradation of Pt and Carbon Support in Polymer Electrolyte Fuel Cell Using Combined Nano-X-ray Absorption Fine Structure and Transmission Electron Microscopy Techniques, *ACS Appl. Mater. Interfaces* **2018**, *10*, 27734-27744.
61. Wang, D.; Xin, H. L.; Hovden, R.; Wang, H.; Yu, Y.; Muller D. A.; DiSalvo, F. J.; Abruña, H. D. Structurally Ordered Intermetallic Platinum-Cobalt Core-shell Nanoparticles with Enhanced Activity and Stability as Oxygen Reduction Electrocatalysts, *Nat. Mat.* **2012**, *12*, 81-87.
62. Mayrhofer, K. J. J.; Viktorija, J.; Katrin, H.; Marianne, H. Matthias, A. Adsorbate-Induced Surface Segregation for Core-Shell Nanocatalysts, *Angew. Chem. Int. Ed.* **2009**, *48*, 3529-3531.
63. Chen, S.; Sheng, W.; Yabuchi, N.; Ferreira, P. J.; Allard, L. F.; Shao-Horn, Y. Origin of Oxygen Reduction Reaction Activity on "Pt₃Co" Nanoparticles: Atomically Resolved Chemical Compositions and Structures, *J. Phys. Chem. C* **2009**, *113*, 1109-1125.
64. Nakamura, M.; Nakajima, Y.; Hoshi, N.; Tajiri, H.; Sakata, O. Effect of Non-Specifically Adsorbed Ions on the Surface Oxidation of Pt(111), *PhysChemPhys* **2013**, *14*, 2426-2431.

65. *XAFS Techniques for Catalysts, Nanomaterials, and Surfaces* (Iwasawa, Y., Asakura, K., Tada, M., Eds.), Springer, Nov. 2016.
66. Ravel, B.; Newville, M. ATHENA, ARTEMIS, HEPHAESTUS: Data Analysis for X-ray Absorption Spectroscopy using IFEFFIT. *J. Synchrotron Radiat.* **2005**, 12, 537-541.
67. Rehr, J. J.; Albers, R. C. Theoretical Approaches to X-ray Absorption Fine Structure, *Rev. Mod. Phys.* **2000**, 72, 621-654.

Graphical table of contents

